UNIVERSITÀ
DEGLI STUDI
DI BRESCIA

Dottorato di Ricerca in

Ingegneria Meccanica e Industriale

Settore Scientifico Disciplinare

ING-IND/10 - Fisica Tecnica Industriale

CICLO XXXIII

CFD analysis of a vacuum microgripper

Dottorando:
Dario Giuseppe Urbano
f.to digitalmente ex art.24 D.Lgs. 82/05

Relatore:
Ch.mo Prof. Adriano Maria Lezzi
f.to digitalmente ex art.24 D.Lgs. 82/05

Acknowledgements

Ringrazio il Professor Adriano Maria Lezzi per il supporto, gli insegnamenti e la fiducia mostratami durante questi tre anni di ricerca. Un ringraziamento speciale al Professor Antonio Ghidoni e al Dr. Gianmaria Noventa per l'aiuto, i suggerimenti e soprattutto la disponibilità mostrata durante lo svolgimento del lavoro computazionale: le vostre critiche e osservazioni hanno contribuito a dare valore aggiunto a questo lavoro.
Ringrazio tutti gli amici e colleghi del dottorato che hanno condiviso con me questo percorso, in particolare: Andrea Aquino, Arianna Bonzanini, Buket Boz, Marco Demori, Marco Ferrari, Alessia Fracassi, Gianmaria Noventa, Luigi Polonini, Laura Tocci.
Grazie ai miei genitori, ad Alessandro, Chiara, Luca e al piccolo Leonardo.

Table of contents

List of figures

List of tables

Nomenclature

Roman Symbols

l_1	Distance between gripper bottom wall and air inlet axis
l_2	Distance between gripper bottom wall and the releasing mass
l_3	Distance between the downstream releasing mass basis and the outlet
$\dot{m}$	Mass flow rate computed by CFD simulation on half gripper volume
$\dot{m}_0$	Mass flow rate through the gripper cannula
$\dot{m}_1$	Mass flow rate entering throught the two lateral holes
$\dot{m}_2$	Mass flow rate at the outlet section
D	Gripper body inner diameter
d	Lateral hole inner diameter
k	Turbulent Kinetic Energy
L	Releasing mass lenght
L_{tot}	Total microgripper length
p_{01}	Stagnation pressure at inlet section
Tu_1	Turbulence intensity at inlet section
T_{01}	Stagnation temperature at inlet section

Acronyms / Abbreviations

CFD	Computational Fluid Dynamics

CFL Courant-Friedrichs-Lewy number

DOE Design of Experiments

LES Large Eddy Simulation

MEMS Micro Electro Mechanical Systems

OLS Ordinary Least Squares method

RANS Reynolds Average Navier Stokes

RG Reference geometry

URANS Unsteady Reynolds Average Navier Stokes

Abstract (in Italiano)

La crescente corsa alla miniaturizzazione ha interessato negli ultimi decenni diversi settori tecnologici e continuerà ad avere nei prossimi anni importanza crescente. In questo secolo si è infatti assistito ad una drastica riduzione delle dimensioni dei componenti elettronici in diversi prodotti finali, anche di uso quotidiano (smartphone,pc). Nell'elettronica e nell'informatica questa tendenza è stata ed è ancora oggi particolarmente evidente: la dimensione dei transistor nei circuiti integrati, a partire dal 1960, è diminuita grossomodo di due ordini di grandezza nell'arco di ogni decennio successivo. Questo ha consentito di incrementare il numero di transistor per singolo chip garantendo velocità di calcolo sempre più elevate. Se l'industria elettronica è stata pioniera nel campo della miniaturizzazione, oggi questa tendenza è dominante anche in altri settori, quali, ad esempio, la microsensoristica, la microchirurgia e la biotecnologia. L'esigenza sempre più stringente di affacciarsi al "micro" mondo ha reso necessario concepire e progettare dispositivi che siano in grado di manipolare, assemblare e posizionare oggetti sempre più piccoli (dell'ordine dei micron) in spazi sempre più ristretti e con sempre maggiore precisione e affidabilità, chiamati *microgrippers*. Diverse tipologie di *microgrippers*, basati su principi di funzionamento differenti, sono stati progettati dalla tecnica e vengono oggi utilizzati diffusamente. Tra questi i *vacuum microgrippers* sono ampiamente utilizzati nell'industria elettronica, in quanto, a fronte di un principio di funzionamento semplice, garantiscono buone prestazioni e costi contenuti. Questo lavoro di tesi prende le mosse dall'analisi fluidodinamica di un particolare design di *vacuum microgripper*, provvisto di un dispositivo di rilascio integrato, con l'obiettivo primario di definire delle correlazioni analitiche utili al dimensionamento di massima di questa topoligia di dispositivo.

Abstract

Since the early 2000s the exponential growth of Micro Electro Mechanical Systems (MEMS), has been made possible by increasingly low production costs, which have paved the way to the design of small devices that are able to manipulate and assemble very small objects (at the micro and nanoscale range) with increasing speed and precision, called microgrippers. According to the specific application, different kinds of microgrippers are available and offer the best gripper performance. Among these, vacuum micro grippers have become widespread in the electronic industry due to a simple working principle and to low cost coupled with fast and effective handling and operation. However, as contact grippers, they have to overcome non negligible adhesion forces between the gripper and the handled object that, at this scale range, can prevent the release of the grasped object. The objective of this work is to present empirical correlations that can be used in preliminary design of a vacuum micro gripper with an integrated automatic detaching tool (releasing mass) [1]. These correlations, able to predict mass flow rate and aerodynamic force acting on the releasing mass, should speed-up the design phase, which is now based on a trial and error approach. CFD approach has been employed to obtain values of $\dot{m}$ and F_M on different gripper geometries: these sets of data have been used to build-up the empirical correlations in terms of three geometrical parameters and of the degree of vacuum in the device.

Chapter 1

Introduction

1.1 Thesis outline

The thesis is organized in four chapters, Conclusions and Appendices.
Chapter 1 presents an overview of gripping tools, introducing some general concepts related to manipulation with a focus on gripping devices operating at the micro-scale (microgrippers).
Chapter 2 describes the microgripper device investigated in this dissertation and its working principle. In the last part, the physical problem is described and some CFD results on the reference gripper geometry are summarized.
Chapter 3 introduces, in the first part, the proposed CFD-DOE approach, describing how it can help to speed-up the design process of the device. A first CFD analysis conducted on different gripper geometries (in the following indicated as "RANS1") is then presented and results are discussed. Empirical correlations able to predict mass flow rate and aerodynamic force on the realising mass of the gripper are proposed, based on "RANS1" set of CFD results. However an unsatisfactory correlation for aerodynamic force and convergence problems arisen in CFD simulations, made it necessary to investigate and revise the computational model set-up. With this purpose, in the last part, a grid independence analysis on a new set of improved meshes (G2 meshes) and a Large Eddy Simulation (LES), both performed on the reference gripper geometry are presented.
Chapter 4 outlines the final CFD analysis: a new type of meshes (G4) was designed and new simulations were carried out. Flow fields and trends analysis are addressed here. Moreover, final empirical correlations for both mass flow rate and aerodynamic force are provided. Finally conclusions are discussed in Chapter 5. Appendices A, B, C, D and E give additional information about previous analysis and numerics.

1.2 Gripping devices

Grippers are the final part of an automated handling system and represent the interface between the handling machine and the object to be grasped.

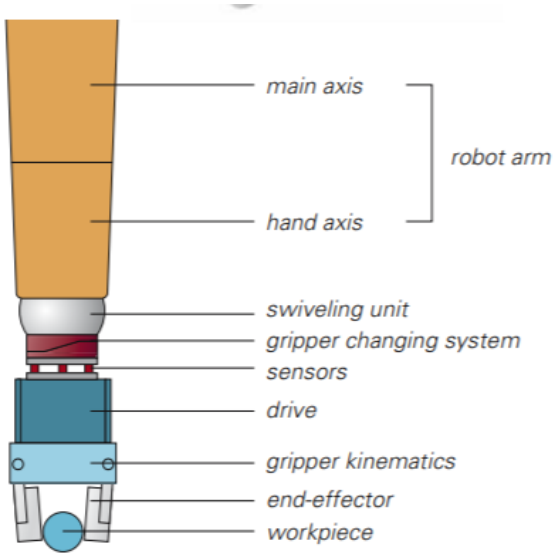

Fig. 1.1 A schematic view of gripper arm and its components

Being the fundamental device which is connected with the working environment, it is evident that its design is crucial to provide an effective handling.
The successful grasping execution is recognized as being one of the most important part in robotics technology applied to industrial applications, where grasp failure can lead to a drastic reduction of production rate and, in same case, also to part damage.
The main manipulation tasks a gripper has to accomplish can be described as follows:

- to correct approach the object and to assure a proper contact
- to maintain a definite position and orientation of the part by exerting forces and moments
- to assure an effective and safe release of the object when it is required

All these functions are deeply affected by several issues and aspects that must be carefully taken into account during a gripping tool design. First of all, part characteristics such as dimensions, weight and physical properties (e.g. flexibility, deformability), but also environment conditions (e.g. temperature, humidity), specific task requirements and

system constrains can significantly influence the grasping process and thereby add additional complexity to the gripper design.

In order to meet different requirements and to solve specific problems arising by particular applications, several types of grippers, based on different grasping principle, have been designed. It should be noted that the "grasping principle" is conceptually different from the "gripper actuation principle". The grasping principle, indeed, can be defined as "the physical principle that causes the force effect necessary to get and maintain the part in a relative position with respect to the gripping device" [2]. The gripper actuation principle, instead, is how the given grasping principle is carried out in the specific gripping tool. The same grasping principle can be so applied in different types of grippers. As an example, the friction between the object and the gripper itself (friction-based gripper) is exploited as grasping principle both by a classical gripper finger, but also in grippers which used fingers in shape memory alloys (SMAs).
In Figure 1.2 some of the most used grasping principles are presented.

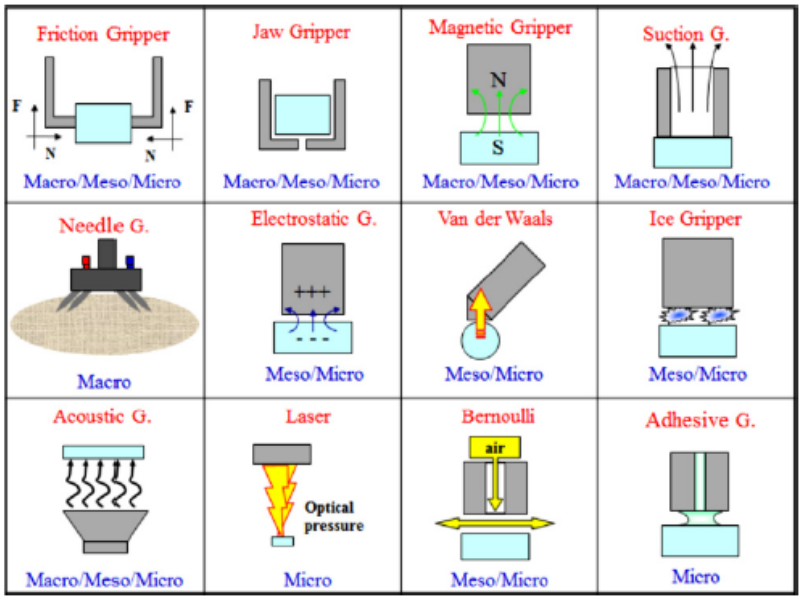

Fig. 1.2 Grasping principles [3]

The oldest friction-based grippers, classically employed in macro-manipulation (part size greater than 10 μm) are mechanical grippers. They usually consist of two or more fingers or jaws which are able to act synchronously to grasp the part. Despite a quite complicate design, they can provide a reliable operation and good adaptability. At the same class belong so called ingressive grippers, which are usually employed to handle objects made by fibrous materials (e.g. textile, carbon or glass fibre) exploiting "pins" which can penetrate the material surface

or simply pinch the object to provide a non-intrusive prehension.
The so called "astrictive grippers" refers instead to that kind of grippers that can apply a continuous holding without provide a direct contact with the object. To this class belong magnetic, electrostatic or vacuum grippers.

Although some of the aforementioned grasping principles can be used in the micro-domain as well (e.g magnetic gripping [4], friction-based gripping [5], suction-based gripping [6]), the increasing complexity needed when handling micro-objects, has required to design grippers based on new and more sophisticated working principles.
The manipulation of micro-parts will be dealt with in more detail in the next subsection.

1.3 Microgrippers

The term "micro-manipulation" has come to be used to refer handling of parts with dimensions ranging between few micrometers and about one millimeter.
In the last decades, that field has been gaining much interest due to the rush to miniaturization of components and final products that nowadays is a general trend throughout the industry. The first studies on the handling of micro-parts were carried out since the early 1990s, but it is only ten years later that micro-manipulation started to be a key issue in scientific and engineering activity. In the early 2000s, indeed, the increasingly low production costs of micro-electromechanical systems (MEMS) caused an exponential growth in the production of micro-devices. Examples include microphones, sensors (e.g. pressure, flow, IR sensors), switches, tunable filters and inkjet printer heads.
The need to produce a huge number of micro-devices led to the necessity of design a new class of grippers that were able to pick and place microscopic parts, hardly visible if not with the help of microscopes, in a safe and effective way, called microgrippers. Some types of microgrippers exploit and re-adapt grasping principles already widely used in the manipulation of larger objects: magnetic and vacuum microgrippers, are one of the most used. Alongside these, new and more sophisticated grasping principles, such as acoustic [7], cryogenic [8], surface tension [9] have been adapted to create micro-grippers capable of responding to the new challenges posed by manipulation in the micro-world. To create a micro-handling tool is actually a demanding task that is more complex than simply scaling down the overall dimensions. When passing from the handling of macro-objects to the prehension of parts in the micro and nano domain, indeed, one has to deal with several new issues that must be faced at the different phases of the device development.
The first problem concerns the action of adhesive forces that, if they can be neglected in the macro handling, play instead a determining role at these spatial scales. Indeed, when the part

dimensions are less than 10 μm the importance of the adhesion forces (proportional to the object surface) arises and can be dominant on gravitational and inertial forces (proportional to the object volume) (see Figure 1.3).

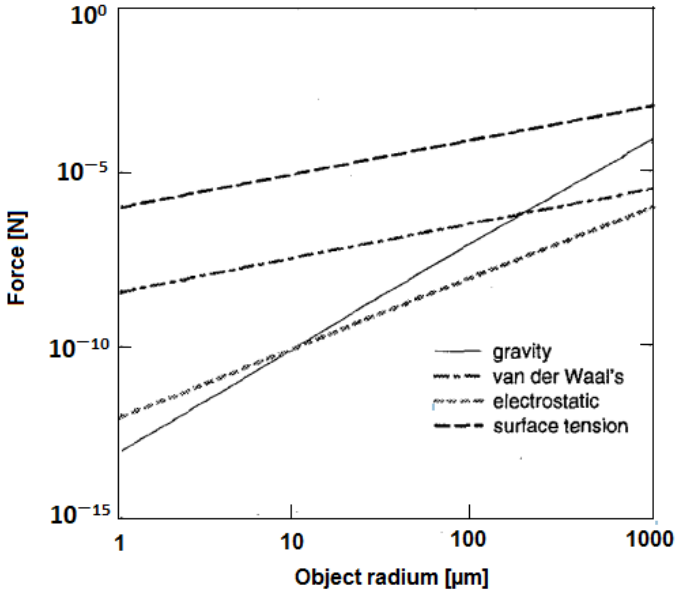

Fig. 1.3 Gravitational, electric, Van der Waals and forces tension forces [10]

This aspect can deeply affect and hinder the correct functioning of a micro–gripper. The main adhesion forces acting in micro-handling are:

- **Van der Waals forces**: indicates a complex of intermolecular force that can occur in different ways between the object and the micro-gripper. The strength of these forces is closely linked to the kind of material interacting.
- **Tension surface forces**: they result from layers of adsorbed humidity on gripper and parts surface. The cohesion forces between the liquid molecules are responsible for the phenomenon known as surface tension. It occurs because the liquid surface has higher energy than its interior. Therefore, the working enviroment humidity must be constantly supervised.
- **Electrostatic forces**: they are related to the Coulomb interaction that occurs between electrically charged bodies. It can be both repulsive and attractive and is more intense the smaller the distance between the two bodies.

During the grasping phase, for instance, as the micro-gripper approaches the object electrostatic interaction between the part and the gripper surface, can lead the part to jump off the

surface into the gripper and misplace, compromising the entire handle operation.
In the release phase adhesive forces can seriously prevent the part detachment from the micro-gripper, because the object tend to stick against the operation tool.
To address this issue, many release strategies have been developed. They can be classified into active and passive systems [11]. Active release strategies consist of additional actions provided to facilitate object detachment in the release phase. They can act by applying other forces on the object, such as mechanical vibration [12] or positive pressure pulse [6]. On the other hand, passive release strategies try to reduce the magnitude of the adhesive forces by various means. Micro-gripper surface can be covered with a conductive layer to prevent electric charge storage [13] or hydrophobic coating [14] from preventing humidity adsorption. Furthermore, grippers made using rough surfaces can reduce the contact area and improve detaching performance. It should be noted that often more than one release strategy is applied at the same time. An overview of the mainly used release strategies is shown in Figure 1.4.

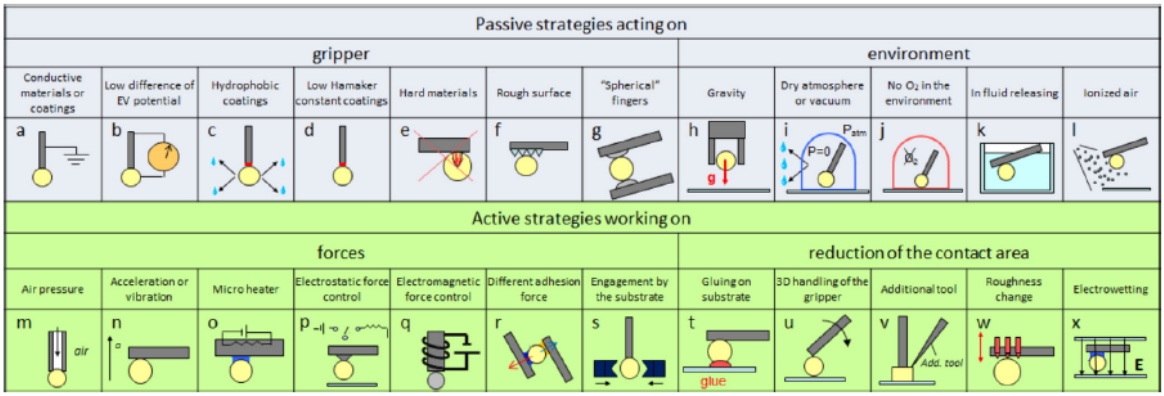

Fig. 1.4 Release strategies [3]

In the following chapter is described the vacuum microgripper design considered in this thesis work.

Chapter 2

Vacuum microgripper physical and computational model

2.1 Rapidograph

In the field of micromanipulation,vacuum microgrippers are widely used, as they are based on a simple operating principle and are low cost. A classic vacuum microgripper consists of two parts: a hollow body and a thin cannula. The operating principle is simple: when a pressure difference, Δp, is created by a vacuum pump between the inlet section and the volume inside the gripper, an airflow is forced through the cannula and into the device, generating a suction force that grabs the object.

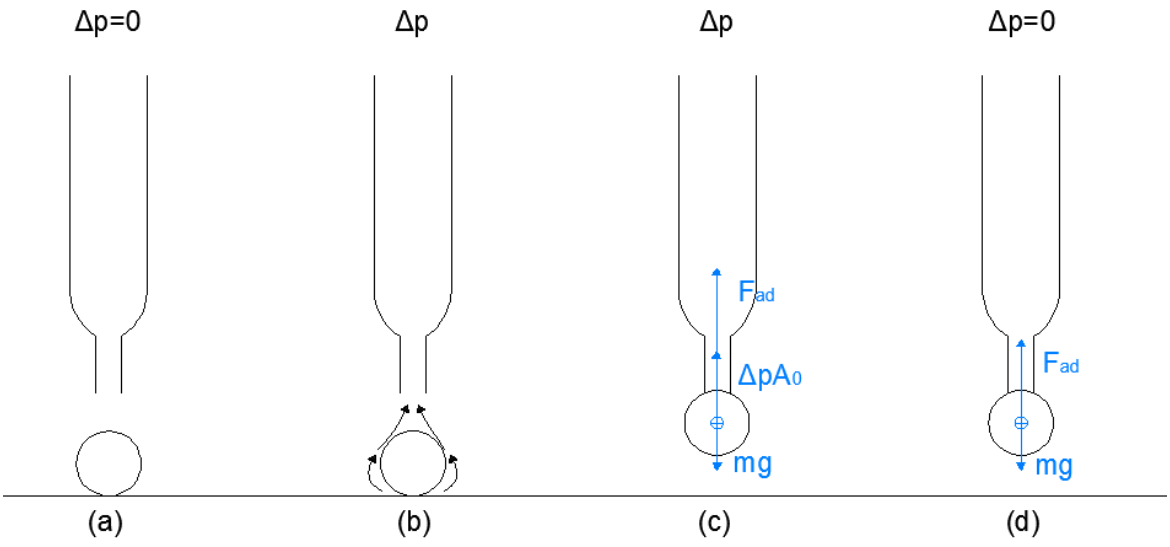

Fig. 2.1 Off (a), Grasping (b), Handling (c) and Releasing (d) manipulation phases in a classic vacuum microgripper

When the object sticks against the cannula end (holding phase) (Figure 2.1c), the gripper must provide a continuous holding force (F_H) that, according to Equation 2.1, must be sufficiently high to overcome the weight force minus adhesion forces (F_{ad}):

$$F_H = \Delta p A_0 \geq mg - F_{ad} \tag{2.1}$$

where A_0 is the cannula cross section area, m the object mass and g = 9.81 m/s² the gravitational acceleration.

The release phase begins when $\Delta p = 0$. However, the gravitational force is often not large enough to pull the object away precisely because of the aforementioned adhesive forces acting between the object and the surface of the cannula.

Some release strategies typically employed in vacuum microgrippers involve the use of mechanical vibrations [12] or more frequently exploit a pressure inversion (positive pressure pulse) that pushes the object away. Although both of these solutions increase the efficiency of the release, they make the handling of the object more complex and, therefore, more expensive, as well as they increase the risk of displacement of the object after the release.

To overcome these issues, a new design of vacuum micro-gripper has been presented and patented by the Department of Robotics Engineering of the University of Brescia. The ultimate goal was to design a gripping device by implementing a release strategy that would be effective without overcomplicating the gripping operation. The idea was to use a Rapidograph® (which is a technical pen created for engineering and architecture drawing) nibs as a gripper end-effector.

The Rapidograph® design, shown in Figure 2.2, features a unique ink release mechanism. Inside the nib structure, a needle, topped with a cylindrical weight (from now on referred to as "releasing mass"), is placed inside a hollow cannula and protrudes slightly downward the pen's tip. The release system, consisting of the needle and the releasing mass, is topped with a case where the ink is stored (Ink reservoir). Moreover two lateral holes are provided on the nib's external body (see Figure 2.2). During the normal functioning, as soon as the pen tip touches the paper, the needle and the releasing mass move upward allowing the ink to be released.

The same mechanism can be effective to help the object detachment, when the Rapidograph® nib is used as the end-effector of a vacuum micro-gripper tool (see Figure 2.3).

When a pressure difference is created inside the micro-gripper body, by a vacuum pump, the airflow entering from the cannula and the two lateral holes, letting the object to be grasped. Conversely, as the pressure difference is removed the releasing mass moving down, helping with its weight the object detachment. In the following, the forces acting on the object and the releasing mass at each stage of the gripping process will be analyzed in more detail.

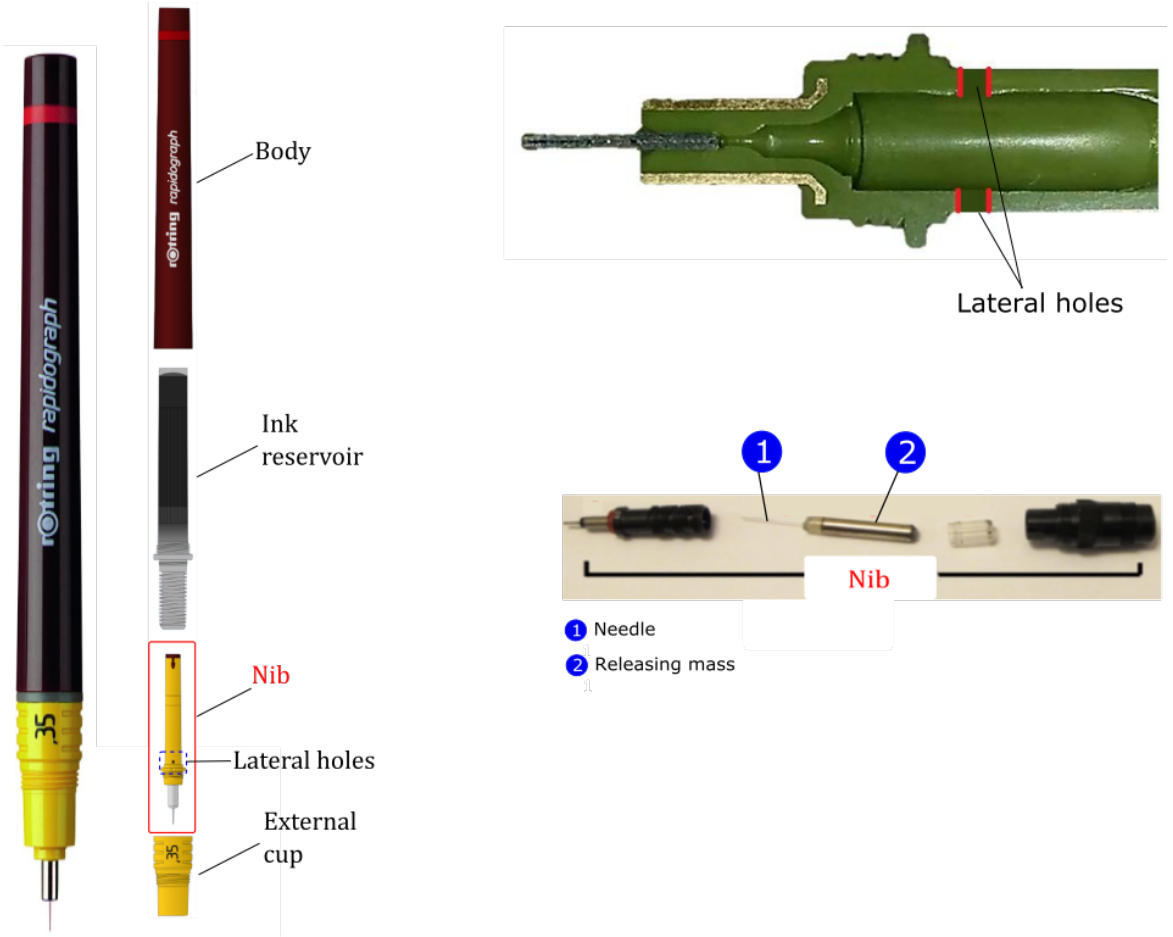

Fig. 2.2 Rapidograph® design: Left: Main Rapidograph® elements - Top right: Photograph of Rapidograph® longitudinal section and details of lateral holes - Bottom right: Elements of Rapidograph®'s nibs

The aerodynamic force (F_M) acting on the releasing mass during the device operation (grasping and holding phase) (Figure 2.3b and Figure 2.3c) is sum of two contributions, according to the following equation:

$$F_M = F_P + F_V \tag{2.2}$$

The pressure force (F_P) is generated by the difference between the average pressure acting on the upstream (p_{sx}) and the downstream (p_{dx}) base of the releasing mass (A_c) and is defined as

$$F_P \cong (p_{sx} - p_{dx}) A_c \tag{2.3}$$

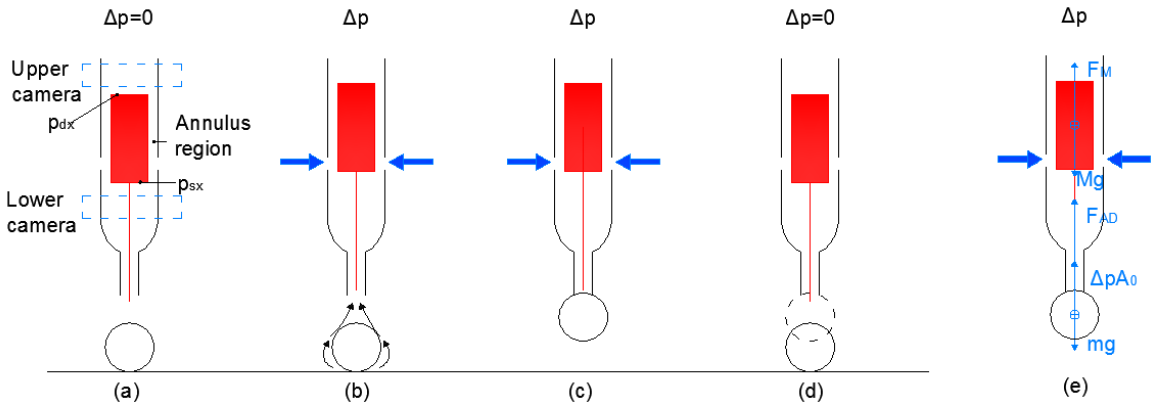

Fig. 2.3 Off (a), Grasping (b), Handling (c) and Releasing (d) manipulation phase of the studied vacuum. Forces acting on the grasped object and the releasing mass during the handling phase (e)

The viscous force (F_V) is generated by the wall shear stress (τ_w) acting on the releasing mass lateral surface (A_L) in the annulus region, and is defined as

$$F_V = \int_{A_L} \tau_w dA \tag{2.4}$$

When the pressure difference is removed, i.e. Δ p = 0, the releasing mass moves downward and help the object detachment (see Figure 2.3d). As shown in [15], the presence of this integrated release tool is able to improve significantly the device release effectiveness. Greater values of the releasing tool mass (M) allow to break higher adhesive forces, especially for smaller objects, according to the following equation:

$$(m+M)\,g > F_{AD} \tag{2.5}$$

The value of M must be carefully chosen (see Figure 2.3e) as follows:

$$M \leq \frac{F_M}{g} - m \tag{2.6}$$

to ensure that F_M is sufficiently high to correctly lift the releasing tool and guarantee a proper device operation. The value of F_M is closely related to the air flow field that develops inside the gripper which, in turn, is strictly affected by the device geometry. This thesis investigate how CFD analysis can be employed to provide an acceptable estimation of F_M, knowing gripper geometry and imposed pressure difference.

2.2 Reference geometry

In a first step, the characteristics of commercially available Rapidograph® nibs were analyzed to identify those that were best suited for use as end-effector of a gripping device. In particular, three models have been taken into account: the *yellow 0.2*, the *white 0.25* and the *green 0.3* (see Figure 2.4). Essentially, the nibs used in these three Rapidograph® models show the same structure and differ only for the hole diameter and the inner needle diameter, as reported in Table 2.1. The same releasing mass is employed in all three pens.

Fig. 2.4 Left: The three Rapidograph® pens - Center: Rapidograph® nibs - Right: The releasing system

Table 2.1 Rapidograph® nibs characteristics

Rapidograph® model	Hole Diameter [μm]	Needle Diameter [μm]	Mass weight [mg]
Yellow 0.2	139	79	707
White 0.25	152	79	707
Green 0.3	208	145	707

The device to be investigated was set up considering the *Green 0.3* model and replacing its releasing system with the one used in the *Yellow 0.2* model. The smaller needle diameter of the *Yellow 0.2* nib, indeed, allows a greater airflow inside the device and prevent the flow from becoming chocked. Since many geometrical configurations will be analyzed throughout this work, we will use the term "reference geometry" to refer to this initial geometry. In Figure 2.5, the main geometrical and physical variables that will be used in this study are

shown. Table 2.2 summarizes geometrical variable values that characterize the reference geometry (more detail on Rapidograph geometry in Appendix A)

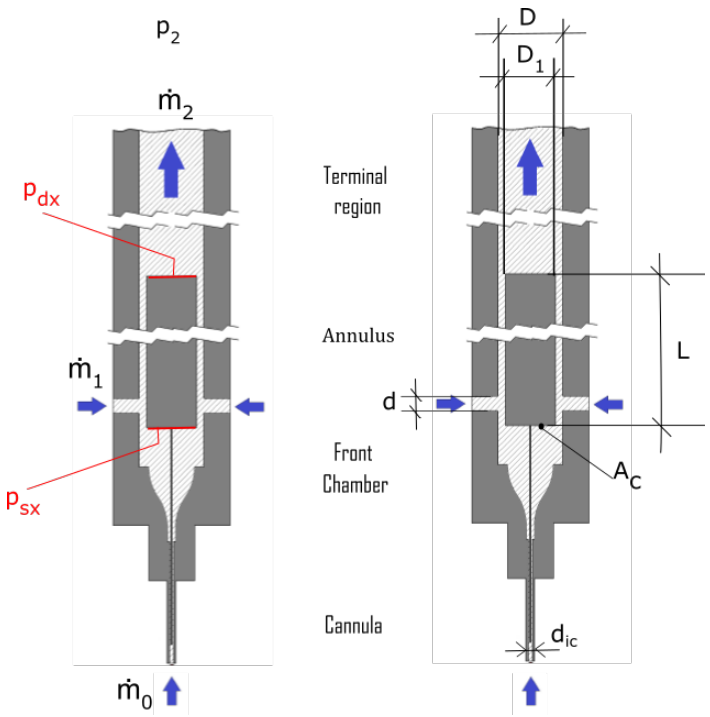

Fig. 2.5 Sketch of the gripper

Table 2.2 Reference geometry main sizes

d [mm]	L [mm]	D [mm]	D_1 [mm]
0.77	24.2	3.4	2.6

2.3 Computational model

The reference geometry of the device was firstly investigated, in order to build up a computational model able to predict properly the flow fields inside the gripper. A previous numerical study of the device [16] shows that the airflow entering through the cannula ($\dot{m}_0$) is very small, two orders of magnitude lower, compared to the one through the lateral holes ($\dot{m}_1$) and therefore, neglecting the presence of the cannula in the simulation, does not affect the prediction of total mass flow rate and aerodynamic force on the releasing mass (for more details on the previous study see Appendix B). As a consequence, in all CFD simulations

reported in this dissertation, the computational domain of the gripper was defined taking into account only the gripper body geometry. In the prototype presented in [17] and [18] a mechanical stop prevents the releasing mass to be lifted beyond an assigned height. In the model for CFD analysis, the releasing mass is considered fixed at the maximum height. The distance between gripper bottom wall and air inlet axis is $l_1 = 3.25$ mm, whereas that between the gripper bottom wall and the releasing mass is $l_2 = 2.1$ mm. The distance between the downstream releasing mass basis and the outlet is $l_3 = 10$ mm.

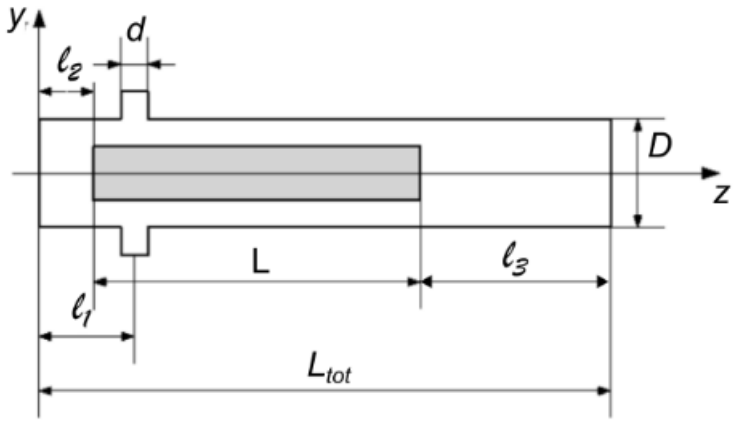

Fig. 2.6 Uncoupled problem

All numerical simulations were computed with the CFD toolbox OpenFOAM® [19]. The k-ω SST turbulence model was employed as well without the aid of wall functions. The convective terms of velocity and energy were discretized with a second order upwind scheme, while for the diffusive terms a linear second-order bounded central scheme was used. The gradient term was evaluated using a center differencing method and the first order upwind scheme approximates the turbulent quantities. Taking advantage of the symmetry with respect to the xz-plane in Figure 2.6, all CFD simulations performed in this work (except for LES) have been carried out of half gripper body.

2.3.1 Mesh

In all CFD simulations, a hybrid type mesh was used to discretize the computational domain. Prismatic layers were adopted near the walls in the boundary layer region, while tetrahedra elements are used to fill the rest of the domain. Four parameters were considered to define the prismatic elements at the wall, affecting the resolution of the boundary layer region: the number of layers (n_L), the thickness of the first layer near the wall (y_1), the total height of prismatic layer layer region (y_{BL}) and a stretching factor value (r). The value of these parameters will be specified for all grids used in this work. The height of the first cell near the

wall (y_1) was always set in order to have a non-dimensional distance y^+, defined in equation 2.7, of around 1.

$$y^+ = \frac{y u_\tau}{\nu} \tag{2.7}$$

where y is the distance between the wall and the first cell center, $u_\tau = \sqrt{\frac{\tau_w}{\rho}}$ is the friction velocity, τ_w the wall shear stress and ν is the kinematic viscosity. A value of y^+ that is not too large ensures adequate resolution of the boundary layer and greater accuracy of the chosen turbulence model (SST k-ω), which, by its nature, is more accurate the more refined the grid at the wall.

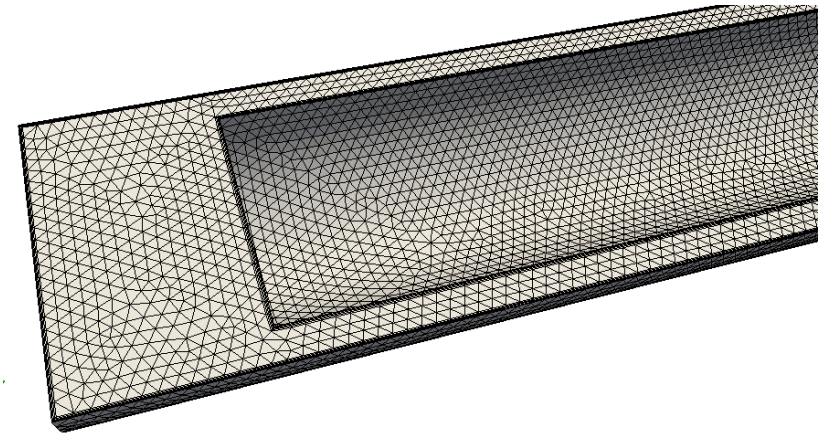

Fig. 2.7 Grid for the reference gripper geometry simulation

2.3.2 Boundary conditions

At the inlet section the value of total temperature (T_{01} = 293.15 K), total pressure (p_{01} = 100 kPa) and turbulence intensity, which is defined by equation 2.8 (Tu_1 = 1%) are imposed and the velocity vector is prescribed to be normal to the inlet patch.

$$Tu = \frac{u'}{\bar{U}} \tag{2.8}$$

$$u' = \sqrt{\frac{2}{3}k} \tag{2.9}$$

$$\bar{U} = \sqrt{\bar{U_x}^2 + \bar{U_y}^2 + \bar{U_z}^2} \tag{2.10}$$

In Equations 2.8, 2.9, 2.10, Tu is the turbulence intensity, u' the root-mean-square of the velocity fluctuation, $\bar{U}$ is the mean velocity and $\bar{U_x}$,$\bar{U_y}$,$\bar{U_z}$ are its components, while k is the turbulent kinetic energy. At the outlet section, the static pressure (p_2) is prescribed.

Symmetry conditions are imposed at the xz-plane (see Figure 2.7) and no-slip wall conditions are defined at gripper body and releasing mass wall. The viscosity is set to $\nu = 1.716 \times 10^{-5}$ $[m^2/s]$.

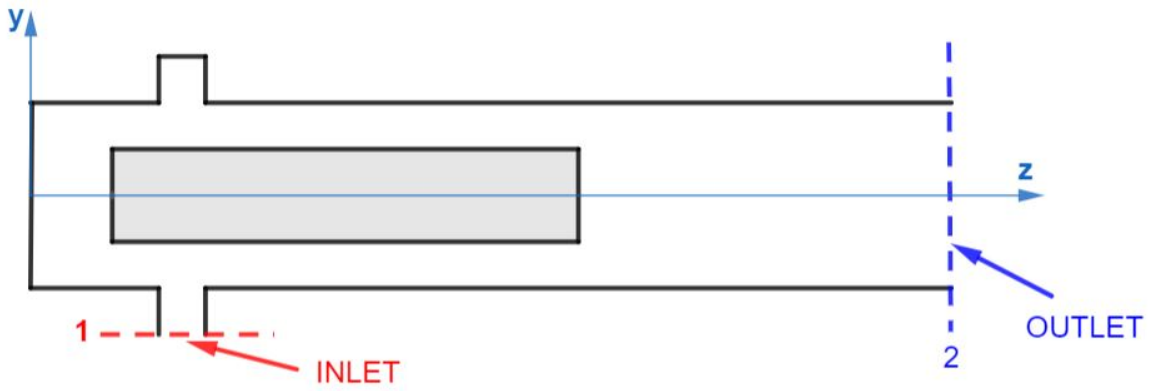

Fig. 2.8 Simplified gripper model for all CFD simulations

2.3.3 Reference geometry: simulation results

This section shows typical pressure and velocity fields obtained from the simulation of the reference geometry, for an outlet pressure of 90 kPa. Only a preliminary analysis of flow fields is presented in this section: the fluid dynamics of the problem will be examined in more depth in Chapter 4. These first results, however, seems to be reasonable according to the physics of the problem.

Fig. 2.9 Velocity magnitude field in the y-z plane - p_2 = 90 kPa (Region close to the outlet not showed in the figure)

Fig. 2.10 Pressure field in the y-z plane - $p_2 = 90$ kPa (Region close to the outlet not showed in the figure)

Fig. 2.11 Temperature field in the y-z plane - $p_2 = 90$ kPa (Region close to the outlet not showed in the figure)

The flow within the micro-gripper is characterized by low velocities, except for the the side-hole region near the inlet (see Figure 2.9), where the Mach number $M_a \approx 0.5$. A Mach number greater than 0.3 typically indicates that the effects of fluid density variation cannot be neglected, which justifies the choice of a compressible solver. The static pressure shows a rapid decrease across the inlet region, while in the annular region, it decreases linearly (see Figure 2.10). The temperature field is nearly uniform throughout the domain (see Figure 2.11). Table 2.3 shows values of mass flow rate and forces provided by CFD simulation.

Table 2.3 Mass flow rate and force values provided by CFD simulation on the reference gripper geometry for outlet pressure $p_2 = 90$ kPa. For an explanation of the name RANS1_RG see picture 3.1.

	$\dot{m}$	F_P	F_V	F_M
	kg/s	N	N	N
RANS1_RG	4.92×10^{-5}	5.91×10^{-3}	8.35×10^{-4}	6.74×10^{-3}

Chapter 3

First set of CFD data: investigation of critical issues

3.1 Introduction

In this and in the next chapter, all the CFD simulations, performed on the several gripper geometries and for different outlet pressures, are presented. The scheme in figure 3.1 summarizes all simulations carried out in this dissertation, grouped in different sets. Two sets of simulations (in what follows referred as RANS1 and RANS4) were performed on different gripper geometries. Simulations denoted as RANS2, RANS3 and LES were indeed performed on the gripper reference geometry (RG) only. Moreover, grids employed in simulations (G1, G2, G3, G4) are indicated as well.

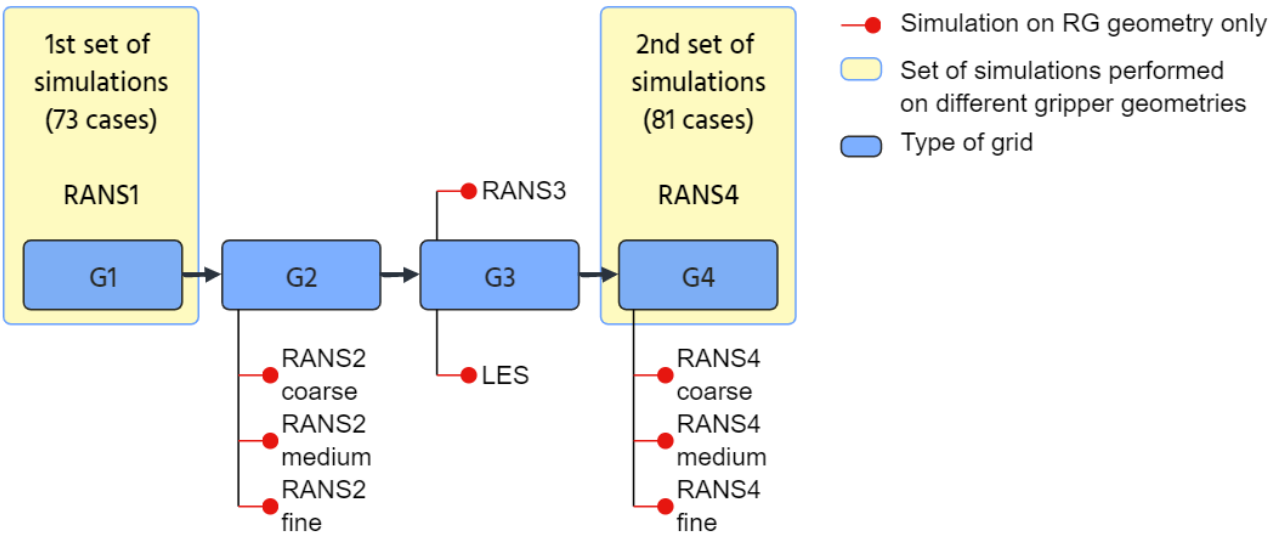

Fig. 3.1 Scheme of all CFD simulations performed

3.2 Gripper design problem and initial CFD study

As it was reported with more details in section 2.1 at page 7, a good design cannot be separated from a proper choice of the releasing mass (M), which is, in turn, strictly related to the value of F_M. On one hand, one can conceive that a larger releasing mass (M) improves the detaching performance of the device, since larger values of adhesion forces can be overcome and, as a consequence, the device is suitable to assure an effective release in handling of smaller parts. On the other hand, a larger releasing mass makes it more difficult to assure a correct lifting of the mass itself during the grasping phase and so can limit grasping performance. Generally speaking, the design of the gripper is framed as a typical design problem, in which it is possible to identify some parameters that can be freely varied inside a proper design space (*design variables*) that affect the quantities we want to investigate (*design responses*). In our problem, mass flow rate and aerodynamic force on the releasing mass represent our design responses. Five parameters, both geometrical and physical, can be firstly assumed as design variables:

- the diameter of the lateral holes (d)
- the length of the releasing mass (L)
- the external diameter of the gripper body (D)
- the imposed pressure difference (Δp)
- the releasing mass value (M)

Once defined, the design variables and the responses, the design problem could be faced through different approaches.
A first technique, widely used in many engineering fields, could be a "trial and error" approach, which can be declined in the following steps:

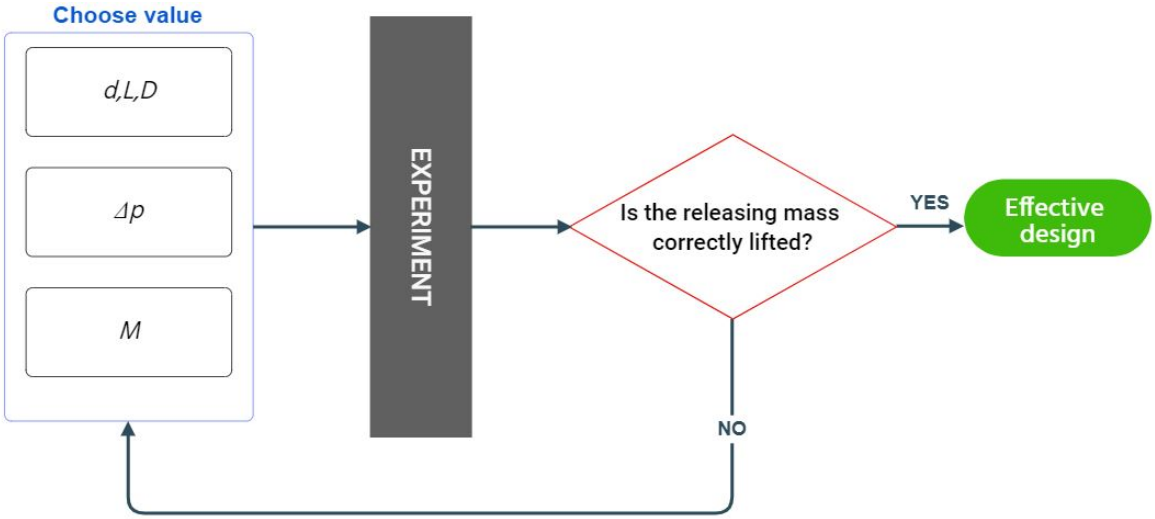

Fig. 3.2 Gripper design: trial and error approach

1. Choose a value for d, L, D
2. Choose a value of imposed pressure (Δp)
3. Choose a value of M
4. To perform an experiment, in order to verify if the device works properly (i.e. verify the releasing mass is correctly lifted by airflow)
5. Repeat the previous steps, changing gripper geometry or value of M, if step 4 fails.

It straightforward to verify that this approach is too expensive: it requires to perform an experimental run for each design we want to investigate. Instead of performing an experiment to evaluate if the chosen design works properly, an alternative approach could be using CFD analysis to predict the aerodynamic force value acting on the releasing mass. In this case, it is not necessary to choose preliminarily the value of M, since it is possible to estimate directly the value of F_M, that depends only on gripper geometrical parameters (d, L, D) and Δp. It is sufficient to select a value of M that satisfy equation 3.1, to be sure the design will work properly.

$$M \leq \frac{F_M}{g} \tag{3.1}$$

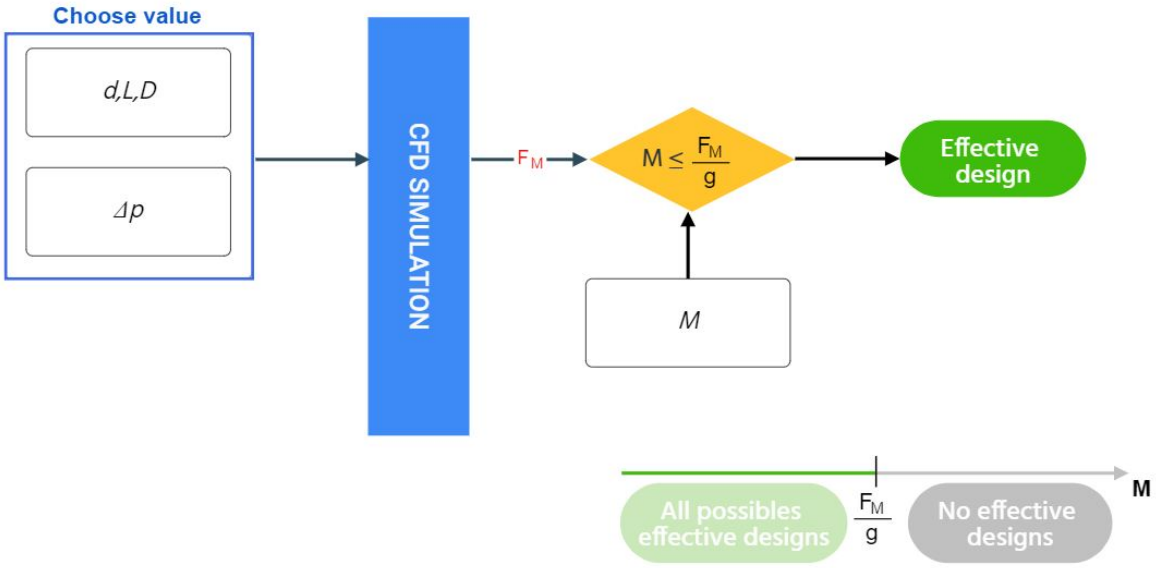

Fig. 3.3 Gripper design: trial and error approach coupled with CFD analysis

As it will be mentioned in more details in the next subsection, this procedure was applied to investigate different geometries of the gripper with a twofold aim. Firstly, to understand how geometrical parameters affects values of $\dot{m}$ and F_M (*sensitivity analysis*) and secondly, use these values, carried out by CFD simulations, to build up empirical correlations, useful to speed up the design process of this kind of device.

3.2.1 Design space definition

The first step to perform a sensitivity analysis was to define for each design variable a set of values to be investigated (*design space*). Starting from the reference geometry (d = 0.77 mm - L = 24.2 mm - D = 3.4 mm) described in section 2.2 (see page 11), we chose to investigate three different values (levels) for each parameter. According to the size of the device, a region of interest and appropriate numerical values have been identified for each level, as shown in Table 3.1.

Table 3.1 Values of design variables

Factors	Level 1	Level 2	Level 3
d [mm]	0.59	0.69	0.77
L [mm]	16.2	24.2	32.2
D [mm]	3.2	3.4	3.6
Δp [kPa]	10	20	30

In particular, d values have been selected in order to reduce the value of the cross section area of lateral holes progressively by 25% for each level, starting from the area of the reference geometry. Similarly, starting from nominal value (L = 24.2 mm), it was chosen to vary the releasing mass length by $\pm$33%. A variation of $\pm$0.2 mm was considered for D value, while three levels of Δp were chosen according to the typical range of operative pressure.

Design of Experiments (DOE) technique was employed to identify which combinations of factor's values should be considered to design a suitable set of CFD simulations. It is a systematic approach, introduced by Fisher [20], for investigating the influence of one or more parameters on experimental runs. One aim of DOE is to set up a design in order to get as much information as possible about the influence of factors on the chosen response variables at the minimal cost. This aspect is crucial in experimental studies, since each experimental run can be very expensive or time consuming. Even if DOE techniques were initially developed to set-up physical experiments, they can be used also for numerical simulations, with a significant computational time saving. Several studies, for instance [21], [22] and [23] have been carried out applying a coupled DOE-CFD approach.

A number of different designs are available to conduct a sensitivity analysis. Full Factorial Design takes into account all the possible combinations of the levels of the factors. Even if this approach can provide a complete information about the design space, it is obviously time demanding since it requires to consider the maximum number of simulations. In Fractional Designs, instead, only a suitable set of parameters' combinations is considered and they represent a good trade-off between computational cost and results accuracy. However, since the number of factors taken into account in our study is not too big, the Full Factorial Design was considered adequate and a set of 81 (=3^4) cases was identified. 27 different gripper configurations, shown in Table 3.2 were investigated for the three outlet pressure value (p_2 = 90 - 80 -70 kPa).

Table 3.2 Gripper geometries identified by Full Factorial Design technique

d	L	D	L	D	L	D
	[mm]					
0.59	16.2	3.2	24.2	3.2	32.2	3.2
	16.2	3.4	24.2	3.4	32.2	3.4
	16.2	3.6	24.2	3.6	32.2	3.6
0.69	16.2	3.2	24.2	3.2	32.2	3.2
	16.2	3.4	24.2	3.4	32.2	3.4
	16.2	3.6	24.2	3.6	32.2	3.6
0.77	16.2	3.2	24.2	3.2	32.2	3.2
	16.2	3.4	24.2	3.4	32.2	3.4
	16.2	3.6	24.2	3.6	32.2	3.6

3.2.2 Automatic mesh generation

For all the 27 geometries, grids have been generated using the open source software SALOME® with the purpose to obtain an acceptable trade-off between computational cost and simulation accuracy. A target number of elements around 1 million was chosen, greater than the value suggested by the grid independence analysis proposed in a previous work [16]. Mesh characteristic are the same already presented in Section 2.3.1.
In order to speed up the grid generation process, an automated approach has been performed using a script written in Python language [24]. At first, the values of geometrical quantities (l_1, l_2, d, D, L, L_{tot}) need to be read by the code to build the CAD gripper geometry. After that, the input mesh parameters (y_{BL}, y_1, n_L, r) are required to mesh the gripper volume automatically.
Table 3.3 summarizes the main characteristics of the grids (in the following referred as "G1") employed in this set of CFD simulations.

Table 3.3 Characteristics of G1 grids

Grid Type	Cells	Boundary Layer			
		y_{BL}	y_1	n_L	r
G1	0.83×10^6	4.20×10^{-5}	8.30×10^{-6}	4	1.15

3.3 Problems

This section examines the problems that occurred running RANS1 simulations, involving both convergence issue and numerical scheme.

3.3.1 Convergence issues

Although the computational analysis conducted on the reference geometry did not show any particular difficulty in the convergence of the calculation (see Section 2.3.3), several instability problems emerged in the simulation on other geometries. Despite efforts to achieve convergence of the calculation, only 45 of the initially planned 81 simulations were successfully completed, as reported in Tab 3.4. To force the simulation to reach a convergent solution, some "tricks" were employed. First of all, it is well known that a good initial condition can help stability and improve the convergence rate, especially if it is not too dissimilar from the expected solution. For this reason, the flow field solution obtained from the computation of a certain gripper geometry was employed as initial condition to simulate the same geometry at a lower value of outlet pressure.

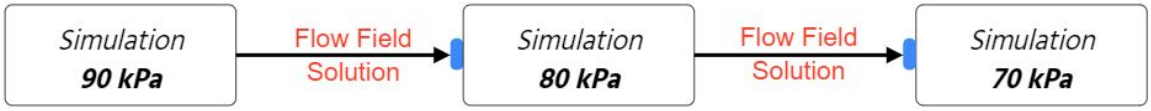

Fig. 3.4 Simulation choice to favour convergence strategy on initial conditions

This strategy allowed to reach a convergent solution in some cases, but convergence issues were still present in the most of the simulations runs. Moreover, to be able to find a convergent solution for low outlet pressure (70 kPa), additional simulations were performed at intermediate values of outlet pressure (p_2) not planned at the beginning. A total of 73 simulations have been performed as shown in Table 3.4.

Table 3.4 Simulation successfully performed for each geometry

d	L	D	p_2				
mm	mm	mm	kPa				
			90	85	80	75	70
0.59	16.2	3.2	●	●	●	●	●
0.59	16.2	3.6	●	●	●	●	●
0.59	24.2	3.4	●	●	●	●	●
0.59	32.2	3.2	●	●	●	●	●
0.59	32.2	3.6	●	●	●	●	●
0.69	16.2	3.6	●	●	●	●	●
0.69	24.2	3.4	●	●	●	●	●
0.69	32.2	3.6	●	●	●	●	●
0.77	16.2	3.2	●	●	●	●	●
0.77	16.2	3.6	●	●	●	●	●
0.77	24.2	3.2	●	●	●	●	●
0.77	24.2	3.4	●	●	●	●	●
0.77	24.2	3.6	●	●	●	●	●
0.77	32.2	3.2	●	●	●	●	●
0.77	32.2	3.6	●	-	●	-	●

3.3.2 Discretization scheme

In order to overcome convergence issues, numerical set-up was adjusted throughtout the 73 simulations. In particular, changing the gradient scheme from the adopted *GaussLinear* to the *LeastSquare* scheme seemed to improve the computation stability and therefore, this approach was employed in those cases where it was more difficult to achieve convergence. This choice was made in the belief that changing the gradient discretization scheme did not significantly influence aerodynamic force and mass flow rate values provided by CFD simulation. However, at the end of RANS1 analysis, this choice was questioned and two CFD simulations on the reference geometry were carried out to verify if gradient discretization scheme could affect values of $\dot{m}$ and F_M. According to results show in Table 3.5, the difference

in prediction of mass flow rate and force values implied that the set of data provided by RANS1 simulations are not homogeneous.

Table 3.5 Comparison of mass flow rate and aerodynamic force value with different gradient scheme (on reference gripper geoemetry at p_2 = 90 kPa)

	GaussLinear	*LeastSquare*
$\dot{m}$ [kg/s]	4.92×10^{-5}	5.21×10^{-5}
F_M [N]	6.74×10^{-3}	6.28×10^{-3}

3.4 Results and empirical correlations

The convergence difficulties shown in this first CFD set of simulations could suggest that the computational model used might not be entirely suitable for studying the fluid-dynamic of the gripper. However, for completeness of analysis, the internal flow fields and the trends of the quantities of interest (i.e. mass flow rate and aerodynamic force) provided by this first set of simulations are presented in this section. For the sake of brevity, values of $\dot{m}$ and F_M provided for all geometries are shown in Appendix C.1.
As expected, the velocity at the inlet increases with the $\Delta p = p_2 - p_0$ across the gripper, as shown in Figures 3.5-3.7-3.9. Figures 3.6-3.8-3.10 show a detail of the zone at the end of the releasing mass. Notice that the recirculation bubble length depends on Δp, increasing for larger Δp. On the outer wall a flow detachment appears, related to the local adverse pressure gradient shown by pressure contours. This adverse pressure gradient is caused by the abrupt increase in cross-section area at the end of the releasing mass that causes the average velocity to drop and as a consequence, the pressure to rise. The detachment is more evident for small Δp, being the flow slower.

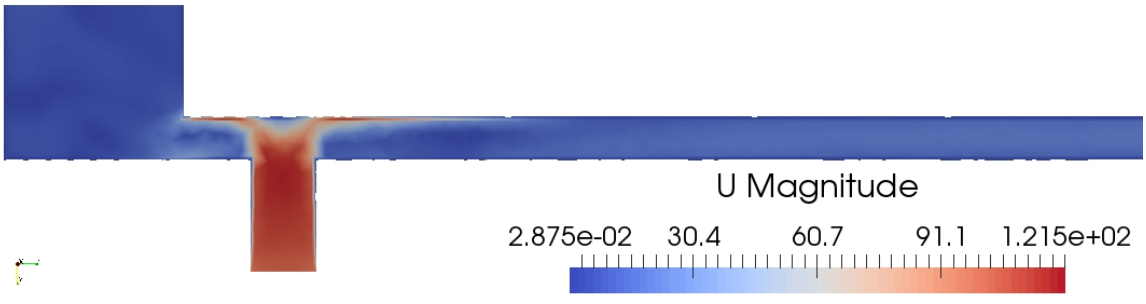

Fig. 3.5 Velocity magnitude contours in the yz-plane d = 0.77 mm, L = 32.2 mm, D = 3.6 mm, p_2 = 90 kPa

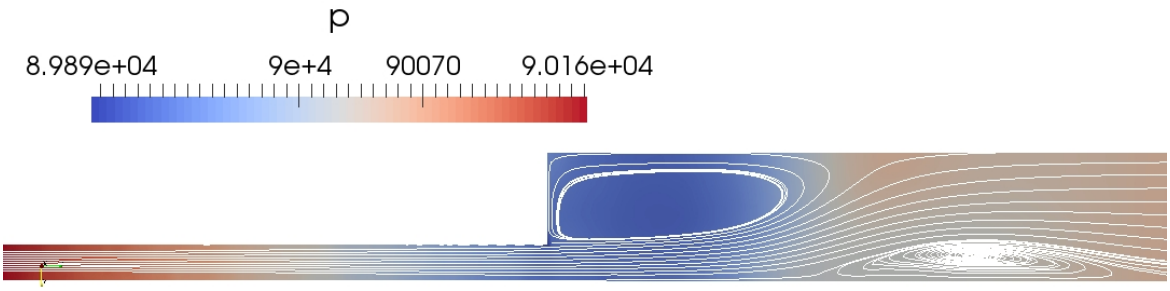

Fig. 3.6 Pressure contours and streamlines in the yz-plane near the end of the releasing mass $d = 0.77$ mm, $L = 32.2$ mm, $D = 3.6$ mm, $p_2 = 90$ kPa

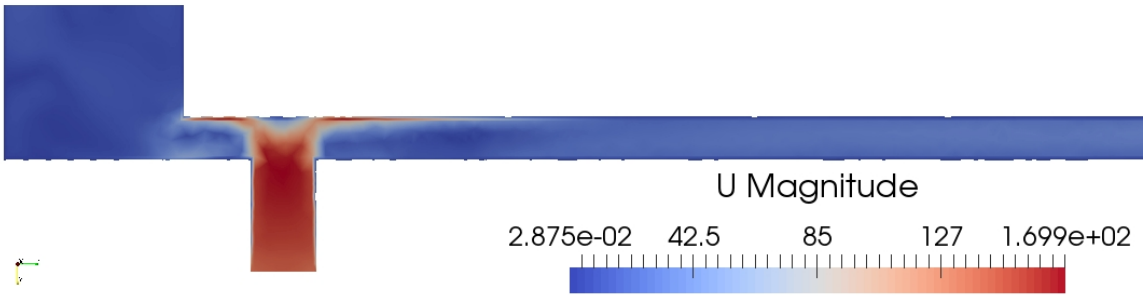

Fig. 3.7 Velocity magnitude contours in the yz-plane $d = 0.77$ mm, $L = 32.2$ mm, $D = 3.6$ mm, $p_2 = 80$ kPa

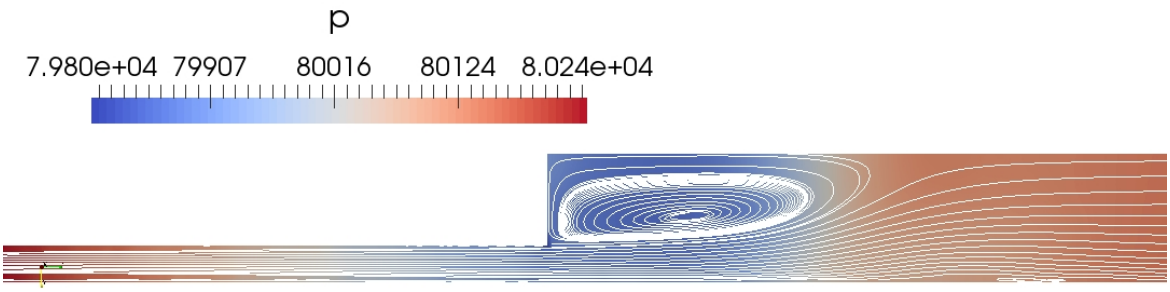

Fig. 3.8 Pressure contours and streamlines in the yz-plane near the end of the releasing mass $d = 0.77$ mm, $L = 32.2$ mm, $D = 3.6$ mm, $p_2 = 80$ kPa

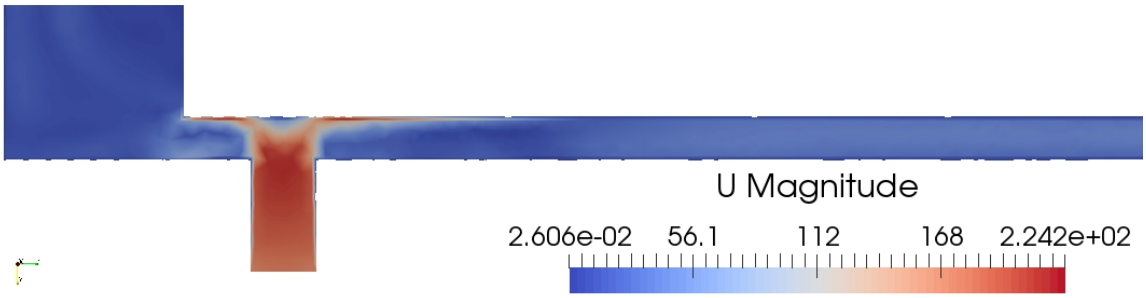

Fig. 3.9 Velocity magnitude contours in the yz-plane $d = 0.77$ mm, $L = 32.2$ mm, $D = 3.6$mm, $p_2 = 70$ kPa

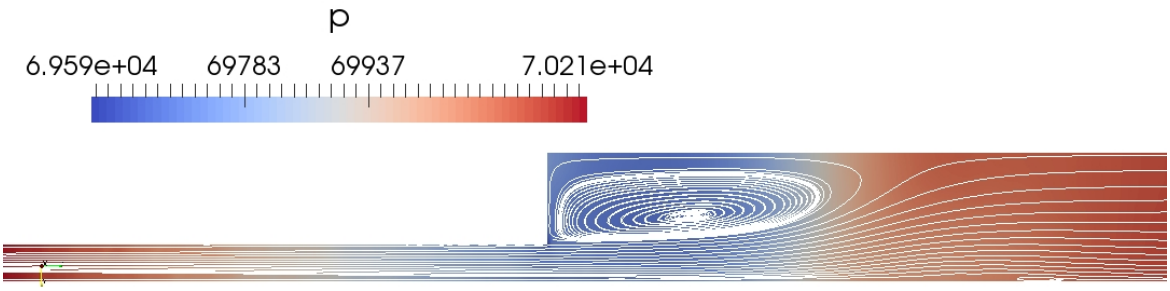

Fig. 3.10 Pressure contours and streamlines in the yz-plane near the end of the releasing mass $d = 0.77$ mm, $L = 32.2$ mm, $D = 3.6$ mm, $p_2 = 70$ kPa

Trend of mass flow rate and aerodynamic force values have been analyzed as well. As expected a larger lateral hole diameter, d, increases the air flow rate flowing through the gripper. Also the aerodynamic force on the releasing mass increases with the hole diameter d (see Figure 3.11). Indeed, a greater air flow rate through the annulus, on one hand increases the shear stresses on the releasing mass lateral surface and the skin friction component, F_V of F_M; on the other hand it causes a larger pressure drop when fluid leaves the annulus, increasing the pressure difference between the two bases of the releasing mass and the pressure component of the force, F_P.
It is interesting to note that force F_M is strongly dependent on the diameter D (see Figure 3.12). In particular, when the value of D increases, force decreases significantly. Both pressure F_P and skin friction component F_V decrease: a greater annulus area reduces shear stress on the lateral surface and the difference of pressure between the basis of the releasing mass. The length of the releasing mass L does not affect the value of mass flow rate appreciably, whereas it has an influence on the value of the lifting force (see Figure 3.13). In particular, the skin friction component increases with L.

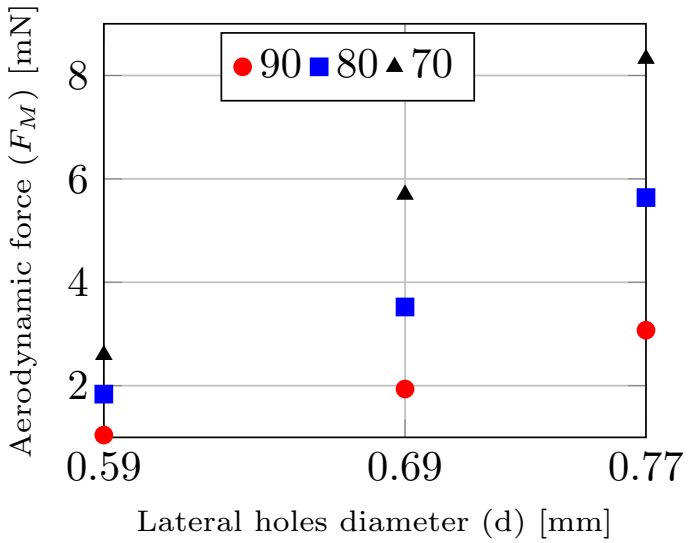

Fig. 3.11 Dependence of aerodynamic force (F_M) on lateral hole diameter (d) at different p_2 values (in kPa)

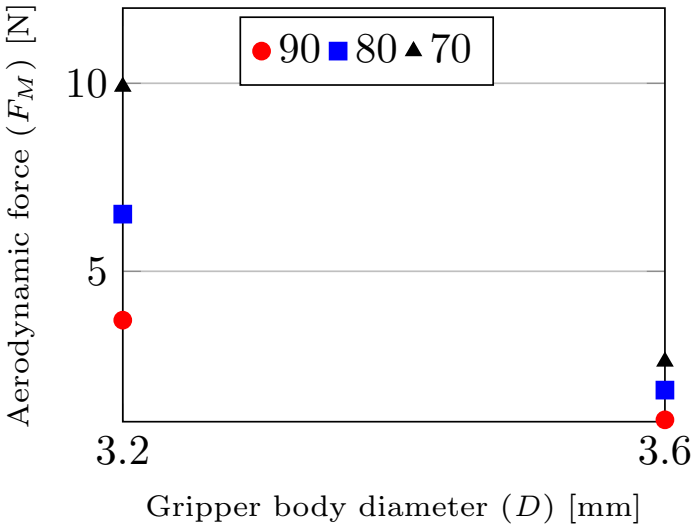

Fig. 3.12 Dependence of Aerodynamic force (F_M) on gripper body diameter (D) at different p_2 values (in kPa)

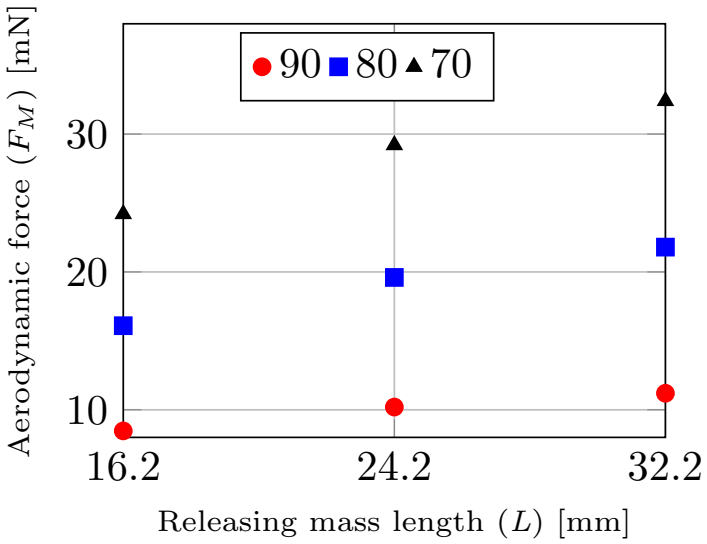

Fig. 3.13 Dependence of aerodynamic force (F_M) on releasing mass length (L) at different p_2 values (in kPa)

Linear regression, based on the Ordinary Least Square (OLS) method, was employed with the help of R software [25] to find empirical correlations able to predict mass flow rate and aerodynamic force given the factors' values. A reliable correlation was found for $\dot{m}$, but the method was not able to identify a good correlation for the prediction of F_M, since it exhibits a too large error (25%). (see Appendix C.2 for more details).

3.5 The road to convergence and to reliable results

Convergence issues emerged in the search for the numerical solution for all geometries, combined with the impossibility of finding, based on the data obtained, a good empirical correlation for the prediction of F_M, lead to think that the computational model adopted taken so far may not be entirely suitable for the study of the problem under consideration and should be improved. In this section, a deeper analysis was implemented in order to improve the computational model.

First of all, the grids used (G1) were investigated more in-depth and an improved mesh (G2) was designed and used to carry out a grid independence analysis. Secondly, a Large Eddy Simulation (LES) was performed together with Dr. Gianmaria Noventa, on the reference gripper geometry: the values of mass flow rate and aerodynamic force supplied by the post-processing of the LES solution, were used as reference to validate how accurate were the RANS simulations provided on G1 and G2 meshes. A new RANS simulation of the reference gripper geometry was performed on the same mesh used for the LES computation

(in the following referred as grid "G3"), to understand if a finer mesh could significantly improve RANS approach accuracy.

3.5.1 Mesh

Meshing phase plays a key role in building-up an accurate computational model and obtaining meaningful and reliable CFD results. Moreover, it is well known how a not proper mesh can heavily affect the solution convergence. To understand how to improve the computational grid, some aspects related to the internal flow of the problem, must be taken into account. First of all, it is important to underline that the main purpose here is to provide a sufficient accurate prediction of the value of the aerodynamic force on the releasing mass (F_M), which represent the main variable for the gripper design. The value of F_M is deeply affected by a good prediction of pressure drop inside the gripper, which depends strictly on how good our computational model is in resolving the boundary layer (BL) in the annular region. With this in mind, a new hybrid unstructured mesh (G2) was generated and used to simulate the reference gripper geometry. In order to resolve more accurately the BL, a greater thickness of the mesh in the BL regions was provided, using a greater number of prismatic layers as well. The total number of elements used are approximately the same of the previous grid (G1) with the same structure: prismatic elements in the BL regions and tetrahedra elsewhere. The main features of the previous (G1) and the new mesh (G2) are listed in Table 3.6. Figure 3.14 shows a detail of BL discretization in the annular region for both grids.

Table 3.6 Comparison between G1 and G2 grids

Grid Type	**Cells**	**Boundary Layer**			
		y_{BL} [mm]	y_1 [mm]	n_L [-]	r [-]
G1	0.83×10^6	4.2×10^{-2}	8.30×10^{-3}	4	1.15
G2	0.78×10^6	10.4×10^{-2}	5×10^{-3}	9	1.15

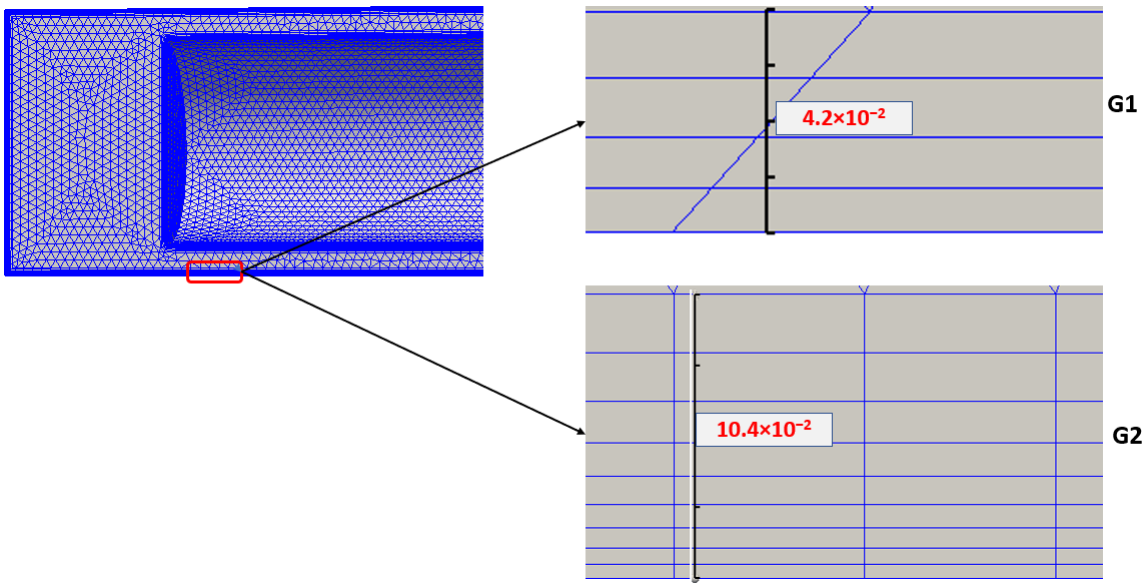

Fig. 3.14 Enlargment of boundary layer region in G1 and new G2 meshes

3.5.2 Grid Independence Analysis

The greater height of the boundary layer in the new mesh G2 should assure a better prediction of the flow fields inside the gripper, since boundary layer resolution seems to have a critical importance for the investigated fluid dynamic problem. Moreover, it should also improve numerical stability, preventing from the possibility the simulation lead to divergence. In order to establish grid independence of the computational model, a comprehensive study on the grid density was carried out. Three level of grid density coarse (0.77×10^6), medium (1.34×10^6) and fine (2.68×10^6) were used to assess the study. Since one of the most important aim is to correctly predict value of mass flow rate and aerodynamic force, the evaluation criteria for grid independence is based on the simulations results of $\dot{m}$ and F_M obtained with the three different meshes.

Table 3.7 summarizes the main characteristic of the three grids used for the grid independence analysis.

Table 3.7 G2 grids for grid independence study

Grid Type	**Cells**	**Boundary Layer**			
		y_{BL} [mm]	y_1 [mm]	n_L [-]	r [-]
G2-coarse	0.78×10^6	10.4×10^{-2}	5×10^{-3}	9	1.2
G2-medium	1.34×10^6	10.4×10^{-2}	5×10^{-3}	9	1.2
G2-fine	2.68×10^6	10.4×10^{-2}	5×10^{-3}	9	1.15

Figure 3.15 shows the variation in $\dot{m}$ and F_M value while increasing the mesh refinement.

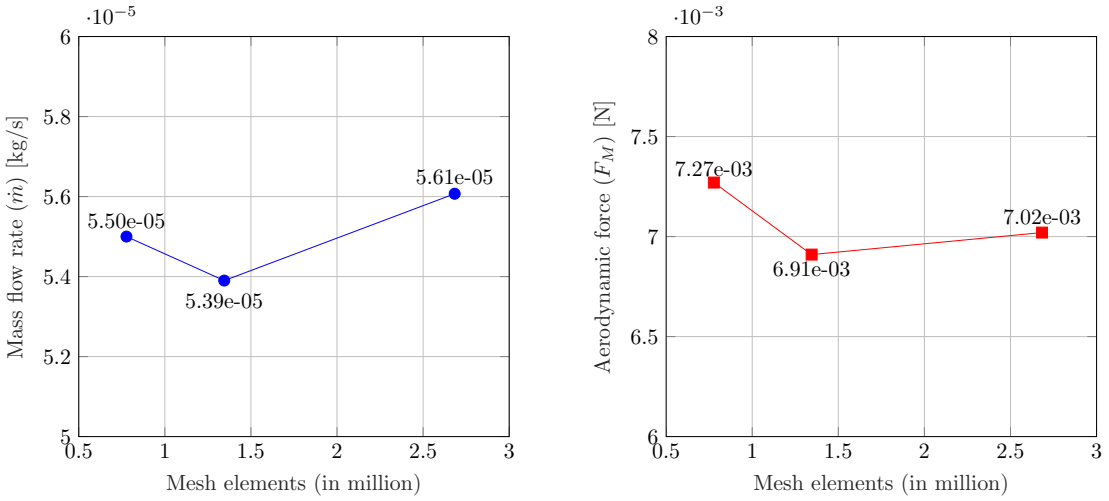

(a) (b)

Fig. 3.15 Grid independence analysis: (a) Mass flow rate ($\dot{m}$), (b) Aerodynamic force (F_M)

It can be seen that, as the number of grid elements increases, the results values do not show a monotonic convergence and therefore a mesh independent solution could not be identified. However, this lack of convergence, is not particular surprising if we analyze in more detail the structure of the three meshes (coarse, medium and fine), involved in the grid independence study. Indeed, starting from the coarse grid, the medium and the fine meshes were obtained by increasing the grid density in the streamwise and spanwise direction, but without changing the grid resolution in the direction normal to the wall. Increasing the grid resolution in the direction normal to the wall could have resulted in a too small y^+ value at the first wall cell (inflation layer) for the fine mesh, leading to convergence issues of the SST turbulence model.

However, this strategy was not appropriate because provided three grids that, even if guaranteed a good resolution in the wall region, appeared, in retrospect, not proper to be used to

perform a grid independence analysis.
Taken together, the findings arisen from this first part of investigation, support the idea that a new grid independence analysis must be provided using a new set of meshes.

3.5.3 LES

Since no experimental tests could be conducted on the gripper and therefore no experimental data of mass flow rate and aerodynamic force were available, a Large Eddy Simulation (LES) was provided together with Dr. Gianmaria Noventa, on the reference geometry to validate the results carried out by RANS approach. It is well known, indeed, that LES is able to capture flow features that cannot be handled with RANS methods and has the potential to provide more accurate results. Moreover, LES can also reveal the presence of unsteady effects in the flow producing more reliable results with respect to an unsteady RANS approach (URANS). The entire volume of the gripper was considered as computational domain for the LES computation, without imposing symmetry condition on the x-z plane (see Figure 3.16).
An unstructured mesh (G3), consisting of 7.67×10^6 cells was employed to discretize the computational domain. Close to the solid boundary, prismatic layers were adopted, with first cell height equal to 5×10^{-3} mm, leading to a maximum non dimensional wall distance y^+ equal to 5.5 at the gripper body wall (see Table 3.8).

Table 3.8 Characteristic of G3 grid

Grid Type	**Cells**	**Boundary Layer**			
		y_{BL} [mm]	y_1 [mm]	n_L [-]	r [-]
G3	7.67×10^6	13×10^{-2}	5×10^{-3}	10	1.2

LES approach have been used directly to resolve the eddies with the larger length scales, while a one-equation eddy viscosity model (kEqn) has been considered as subgrid scale model, to model smaller eddies, using a modeled balance equation to simulate the behaviour of k [26]. The same boundary conditions already used for RANS simulations (see section 2.3.2), were imposed at inlet and outlet sections and at wall boundary. Table 3.9 summarizes solver setting used for LES computation (numerical schemes are reported in Appendix D.2).

Table 3.9 LES computation condition settings

Calculation conditions	**Solver settings**
Computational domain	Entire gripper geometry
Turbulence model	SST k-ω
OpenFOAM solver	rhoPimpleFoam
Eddy viscosity model	KEqn
LES filter type	cubeRootVol
Discretization schemes	Velocity and energy terms: 2nd order upwind scheme Diffusive terms: Linear 2nd order bounded central scheme Gradient term: Center differencing method Turbulent quantities: 1st order upwind scheme
Boundary conditions	Inflow: T_{01} = 293.15 K - p_{01} = 100 kPa - Tu_1 = 1% Outflow: Static pressure (p_2) value imposed x-z Plane: Symmetry plane Walls: No slip

All results obtained from LES were time-averaged and the averaged value of mass flow rate and aerodynamic force were computed over time. An oscillatory trend was noted in the first time-steps, for both two quantities. However, after the initial transient, both mass flow rate and aerodynamic force values tended to stabilize around a constant value as shown in Figures 3.19 and 3.20.

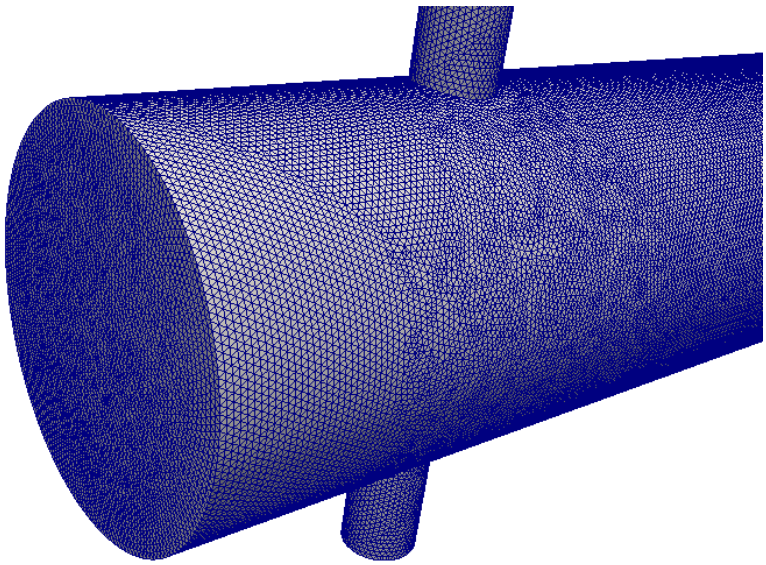

Fig. 3.16 LES computation: Mesh of the computational domain

Figure 3.17 and 3.18 show time-averaged pressure and velocity contours on the y-z plane. The flow-fields obtained with LES, do not show transient phenomena.

Fig. 3.17 LES computation: time-averaged pressure contours in the y-z plane

Fig. 3.18 LES computation: time-averaged velocity magnitude contours in the y-z plane

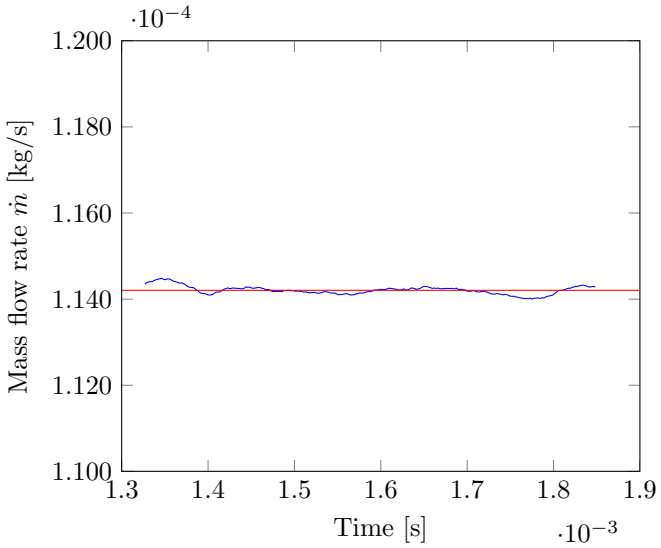

Fig. 3.19 LES computation: Trend of mass flow rate (value on the entire gripper volume)

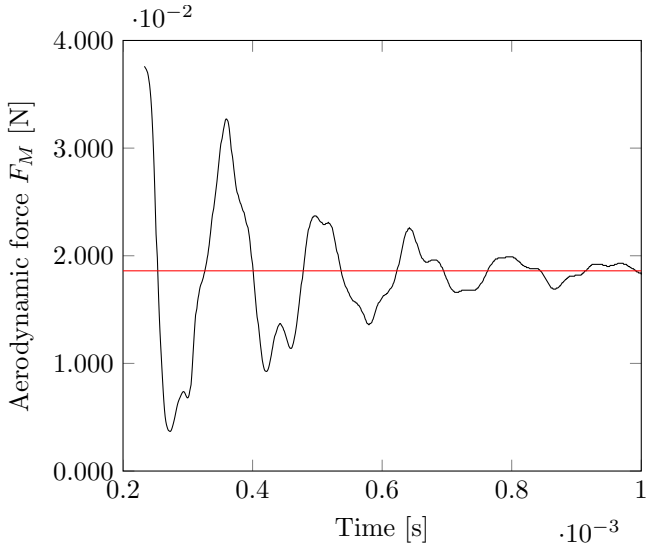

Fig. 3.20 LES computation: Trend of aerodynamic force (value on the entire gripper volume)

Table 3.10 shows the values of pressure ($\vec{F}_P$) and viscous ($\vec{F}_V$) contribution acting on the releasing mass. It is interesting to note how both pressure and viscous components in direction of y-axis (F_{Py} and F_{Vy}) are very small. That confirms the assumption done in all previous simulations, that the flow is symmetric with respect to the xz-plane, since for symmetric flow the value F_{Py} and F_{Vy} should be exactly zero.

Table 3.10 Comparison of the predicted components of the aeodynamic force on the releasing mass for LES approach

	x-axis	y-axis	z-axis
$\vec{F}_P$ [N]	8.75×10^{-5}	9.69×10^{-5}	1.84×10^{-2}
$\vec{F}_V$ [N]	8.34×10^{-6}	7.19×10^{-6}	3.23×10^{-3}

Table 3.11 summarizes the results of LES and RANS simulation, showing a difference around 16% and 38% for the mass flow rate and aerodynamic force prediction, respectively. If the difference in the prediction of mass flow rate value is all in all acceptable and can be ascribed to the intrinsically more accurate LES approach, the significant difference in the force value prediction seems to suggest that RANS approach is not able to supply a reliable estimation of that quantity. However, it is important to note that the big difference in the prediction of force value can be due to the fact two different grids were employed in the two simulations. The LES mesh indeed, in addition to having a greater number of elements, presents also a greater resolution in the BL region. A new RANS simulation (in the following

referred as "RANS3" simulation) was so performed on the reference gripper geometry using the same mesh already employed in LES computation.

Table 3.11 Comparison of RANS1 and LES results: mass flow rate and aerodynamic force

	$\dot{m}$ kg/s	F_M N
RANS	4.92×10^{-5}	6.74×10^{-3}
LES*	5.71×10^{-5}	9.30×10^{-3}

*The values in the table for LES were obtained halving $\dot{m}$ and F_M values carried out by simulation, to refer to half gripper geometry.

3.5.4 Comparison of the RANS and LES results

A new RANS simulation (RANS3) was performed on the reference gripper geometry, using the same grid already employed for the LES, for a comparison between RANS and LES. The solver is the same adopted for the previous RANS simulations (the steady-state *rhoSimpleFoam*), while LES boundary conditions were employed. The results, in terms of $\dot{m}$ and F_M, obtained by this new RANS simulation are show in Table 3.12 and compared with LES results.

Table 3.12 Comparison of RANS1, RANS2 and LES results: mass flow rate and aerodynamic force

	$\dot{m}$ kg/s	F_M N
RANS1_RG	4.92×10^{-5}	6.74×10^{-3}
RANS3	5.29×10^{-5}	8.03×10^{-3}
LES	5.71×10^{-5}	9.30×10^{-3}

As we can see, RANS3 simulation is able to provide a better prediction of $\dot{m}$ and F_M LES values than RANS1. The difference with LES mass flow rate value decreases from 16% (RANS1) to 8% (RANS3). In the same way, the difference on the value of aerodynamic force decreases as well, from 38% to 16%, which is a reduction of more than 50%.
From these data comparison it is argued that RANS approach can be acceptable on the condition to use a sufficiently fine mesh in the boundary layer region.
However, mesh refinement dramatically increases the computational cost, which is a crucial factor to figure out the utility of a CFD solution for our design study. Table 3.13 compares the computational time required to obtain a convergent solution, in the three different simulations

(RANS1, RANS3, LES), employing the same number of processors (i.e. 6). Six processors ware actually employed to run RANS1 simulation on the lab workstation: indeed, this is the optimal number of cores that, according to the number of mesh elements (0.78×10^6) , maximizes the simulation speed. Typically, to have an efficient parallelization a minimum number approximately equals to 1×10^5 mesh cells per CPU processor is required, since lower values lead to a reduction of total simulation speed. For RANS3 and LES a greater number of processors was actually employed to run the simulation (i.e. 136), using the GALILEO supercomputer installed at CINECA [1], while the wall clock time in Table 3.13 was estimated by restarting the computation on the lab workstation.

Table 3.13 Computational time required by simulations

	Mesh Elements	**Type**	**Wall clock time (6 CPU)**
RANS1	0.78×10^6	Steady	3 hours
RANS3	7.67×10^6	Unsteady	5 days
LES	7.67×10^6	Unsteady	6 months

Wall clock time was estimated using 6 processors Intel Xeon CPU E5-2630 2.30GHz

It is trivial to verify that the LES approach is too time demanding to be used to provide simulation of all gripper geometries. The 3D nature of computation, the fine mesh resolution and the necessity to have a very high number of time steps to obtain stable statistics of the flow requires moreover high CPU resources.
RANS3 simulation provides a considerable saving in total computational time compared with LES, but it takes still more time to achieve convergence, due to the fact the same very fine mesh of LES analysis (G3) was employed. As a result, also a RANS approach on a very fine mesh is still impractical to be used to simulate all gripper geometries.
In this scenario, RANS simulations using a coarser grid, appears the most cost-effective approach to be able to predict mass flow rate and aerodynamic force value in all the 81 planned simulations. Although the RANS approach penalizes the accuracy in predicting the value of the force, especially with a coarser mesh, the suggested strategy appears appropriate for our purposes. In fact, to provide a high accuracy in the estimation of aerodynamic force is not the focus of this study. Indeed, our primary goal, is to build-up a computational model able to provide a meaningful data set of force values for the different geometries, that can be used to to derive force empirical correlations. These empirical correlations must be useful to speed-up gripper design and able to give the order of magnitude of the aerodynamic force on the releasing mass.

[1] CINECA is a not-for-profit Consortium and it is the largest Italian computing centre

Chapter 4

CFD analysis and discussion

4.1 Mesh

Previous investigations allowed us to understand how the discretization of the spatial domain is crucial to obtain satisfactory results with a RANS approach. In particular, our goal is to generate computational grids with sufficient resolution to ensure a consistent set of results for the aerodynamic force, based on which we can identify empirical correlations useful to speed-up the design of the gripper. The first group of computation investigation presented in section 3.4, had not allowed to find a good correlation to predict the values of F_M, because of the domain grid that, as demonstrated in Section 3.5.4, was proved unfitted in the boundary layer. To overcome this problem a new grid type (G4) was designed and to identify the optimal mesh density a new grid independence analysis was carried out on the reference gripper geometry. Since our studies suggest that boundary layer resolution is essential for accurate solution, three grids coarse, medium and fine were build-up, using a different refinement level of grid at the walls by halving wall adjacent grid height (y_1). The number of layers in the BL region, was changed in order to have approximately the same BL thickness (y_{BL}) (see Table 4.1).

Table 4.1 Characteristic of grids (G4)

Grid density	Elements	y_1	y_{BL}	n_L	r
Coarse	3.08×10^5	1×10^{-5}	1.64×10^{-4}	8	1.2
Medium	6.79×10^5	5×10^{-6}	1.30×10^{-4}	10	1.2
Fine	15.8×10^5	2.5×10^{-6}	1×10^{-4}	12	1.2

The mesh density in the streamwise and spanwise direction was increased as well with the aim to double the number of total elements from coarse to medium and fine grid. The average mesh spacing adopted are respectively 0.13 mm (coarse), 0.095 mm (medium) and 0.07 mm (fine). Figure 4.1 and 4.2 show the mass flow rate ($\dot{m}$) and the aerodynamic force (F_M), computed using the coarse, medium and fine mesh, respectively. Small differences can be observed between medium and fine meshes for the mass flow rate, while the aerodynamic force does not show a clear grid convergence. However, the difference in the predicted force between medium and fine mesh is below 2%, which can be considered acceptable for this type of study. As a consequence, the medium mesh has been used for all computations shown in the following.

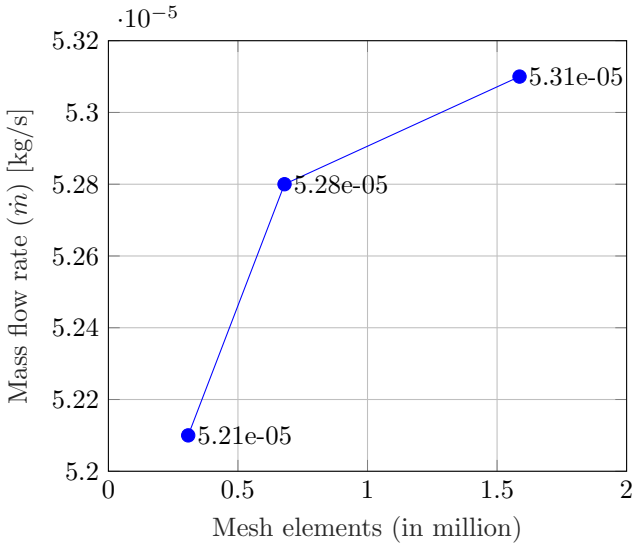

Fig. 4.1 Grid Independence study on G4 grid: Mass flow rate trend

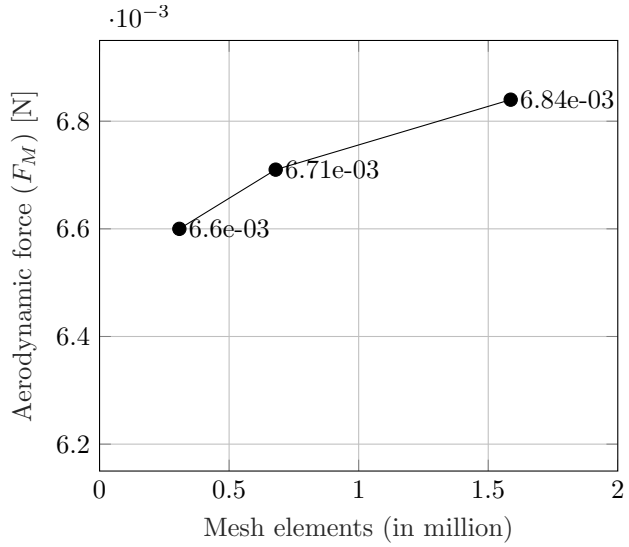

Fig. 4.2 Grid Independence study on G4 grid: Aerodynamic force trend

4.2 Numerical model

The numerical model adopted for these new simulations is essentially the same already employed in the previous CFD analysis, as summarized in Table 4.2.

Table 4.2 CFD simulation condition settings

Calculation conditions	**Solver settings**
Computational domain	Half gripper geometry
Turbulence model	SST k-ω
OpenFOAM solver	rhoPimpleFoam
Discretization schemes	Velocity and energy terms: 2nd order upwind scheme Diffusive terms: Linear 2nd order bounded central scheme Gradient term: Center differencing method Turbulent quantities: 1st order upwind scheme
Boundary conditions	Inflow: T_{01} = 293.15 K - p_{01} =100 kPa - Tu_1 = 1% Outflow: Static pressure (p_2) value imposed x-z Plane: Symmetry plane Walls: No slip

Just as in previous analyses, the steady-state solver *rhoSimpleFoam* based on the SIMPLE algorithm was first considered. However, some stability problems suggested the use of a pseudo-transient method. The unsteady *rhoPimpleFoam* solver, based on the PIMPLE

algorithm, was adopted at the end and the simulation was solved in time with large time steps, making the temporal derivative in equations negligible and drive to reach the steady-state solution. The time-step size was increased setting a high value of the maximum Courant number (CFL) used in the calculus. The higher is the CFL value, the larger is the time step adopted. Since the first stages of calculation are typically characterized by strong transients, the initial CFL value was set to one to mitigate those transient and avoid robustness issues. After first iterations, maximum CFL value was set to 50, sufficiently high to approach the steady state solution quickly.

In addition to the residuals value, another criterion has been defined to check the convergence of the solution. In fact, even if the residuals value reduces by four orders of magnitude, in some case the solution was still oscillating. An algorithm written in Python language [24] was integrated in the CFD code to check runtime a stop condition.
The algorithm operates on successive time intervals $\Delta t_i = 2 \cdot 10^{-3}$ s according to the following steps:

1. For each i th time interval Δt_i, it computes the average value of mass flow rate ($\overline{\dot{m}_i}$) and aerodynamic force ($\overline{F_{mi}}$)

2. Then, it computes the relative change for both mass flow rate and aerodynamic force

$$\Delta \dot{m}_i = \frac{|\overline{\dot{m}_i} - \overline{\dot{m}}_{i-1}|}{\overline{\dot{m}}_{i-1}} \tag{4.1}$$

$$\Delta F_{Mi} = \frac{|\overline{F_{Mi}} - \overline{F_{Mi-1}}|}{\overline{F_{Mi-1}}} \tag{4.2}$$

3. It stops the simulation when both the values of $\Delta \dot{m}_i$ and ΔF_{Mi} fall below a prescribed threshold (i.e. $3 \cdot 10^{-4}$) for the first time.

4.3 Results

In this section, results of the simulations are compared and discussed. In the first subsection, based on the simulations results, flow characteristics inside the gripper, including fluid dynamics structures, pressure and velocity distributions were analyzed. Then, trends of mass flow rate and lifting force in terms of geometrical modification are presented to investigate how geometry affects gripper performance. Eventually, empirical correlations to predict both mass flow rate and lifting force are presented in the last subsection.

4.3.1 Fluid dynamics phenomena

Despite the simple geometry of the gripper the flow structure that develops is rather complex due to the superposition and the interaction among several elementary flows.
Patterns reported here for the reference geometry have been observed in most of the computations. For the sake of simplicity, the gripper inner volume is divided in four region (Front chamber, Jet, Annular and Terminal region) as shown in Figure 4.3.

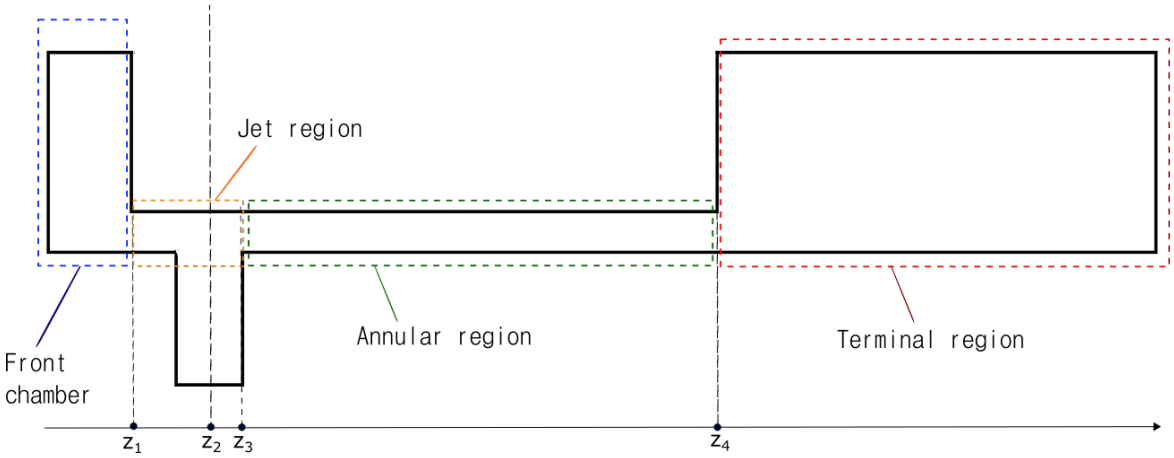

Fig. 4.3 Flow regions

The airflow forced inside the gripper through the lateral hole impinges normally on the releasing mass wall, reaching a peak in static pressure (stagnation point). The jet velocity increases with the imposed pressure (Δp) with a maximum Mach number of 0.78 (for $\Delta p = 30$ kPa and $d = 0.77$ mm): flow is subsonic in all geometrical configurations taken into account. Due to the confined jet impingement on the releasing mass wall, several vortex structures arise in the region nearby the lateral hole, developing along circumferential direction and tending to disappear downstream in the annular region (see Figure 4.4).

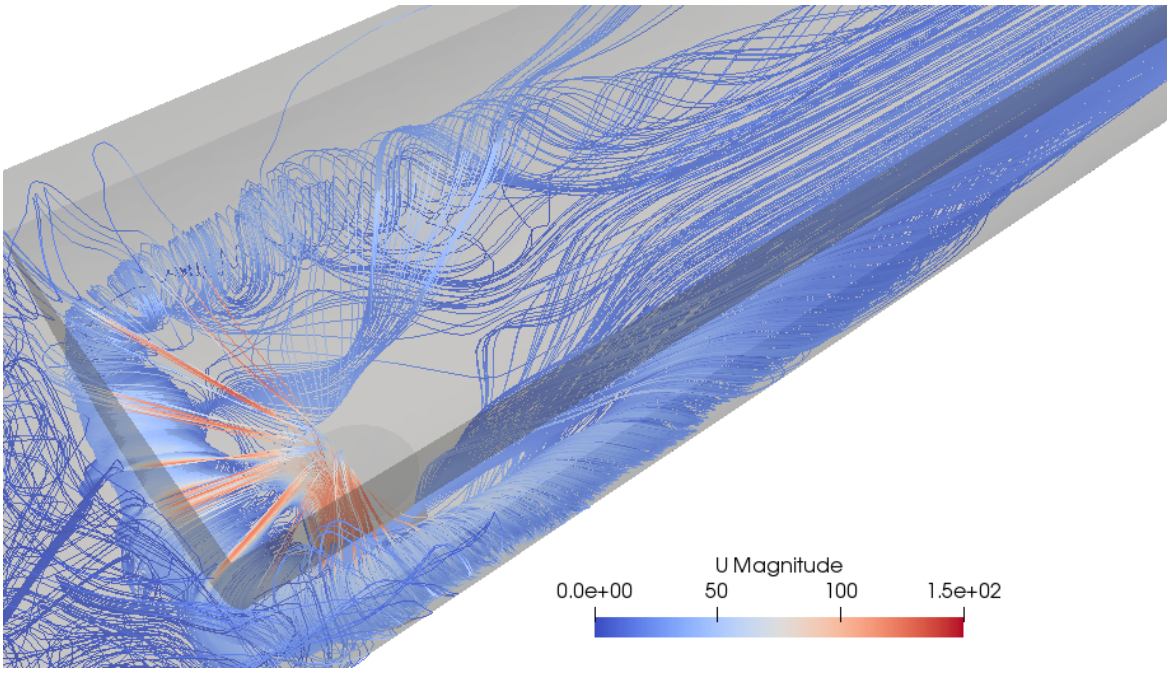

Fig. 4.4 Vortex structures around the releasing mass surface in the first part of the annular region visualized by velocity streamlines (d = 0.77 mm – L = 32.2 mm – D = 3.6 mm)

Figure 4.5 shows vortex structures development at the cross section perpendicular to the gripper axis and passing through lateral jet axis (z_2) for three different gripper geometries. Vortex structures are symmetric with respect to the lateral jet axis, showing different shapes depending on gripper body diameter value (D). A smaller gripper body diameter reduces, indeed, the distance between lateral inlet and the impinging wall surface influencing vortex spatial distribution and the tendency of the flow to stay attached to the cylindrical wall. Other parameters (d, L, p_2) do not have an influence on that.

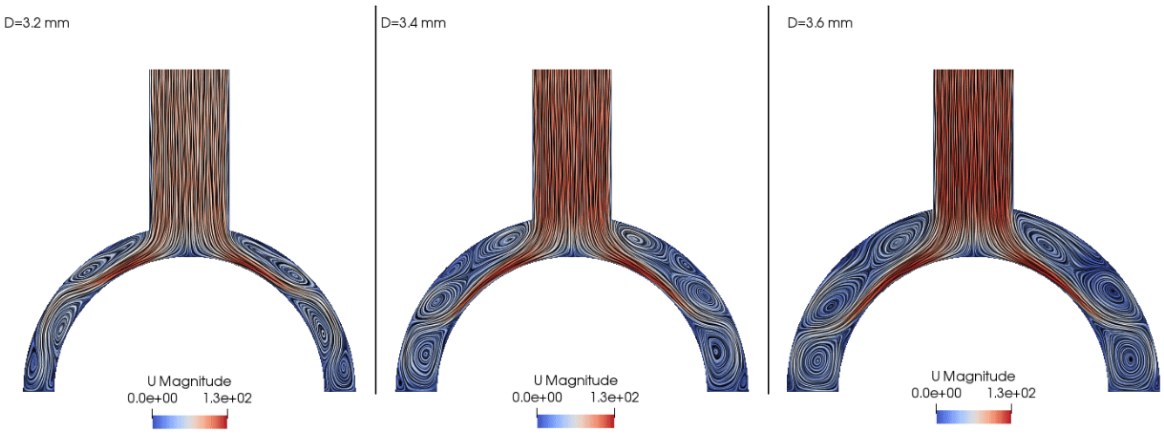

Fig. 4.5 Vortex structures and velocity contour at plane ($z = z_2$) for different gripper body diameter values (D) (reference geometry - $p_2 = 90$ kPa)

Figure 4.6a shows the development of the average value of the static pressure, calculated on cross-sections, along the axis of the gripper. Immediately upstream of the jet, a negative pressure peak can be noted between the front chamber end (z_1) and the lateral jet axis (z_2) as a result of the vortex structure previously discussed (see Figure 4.6b).

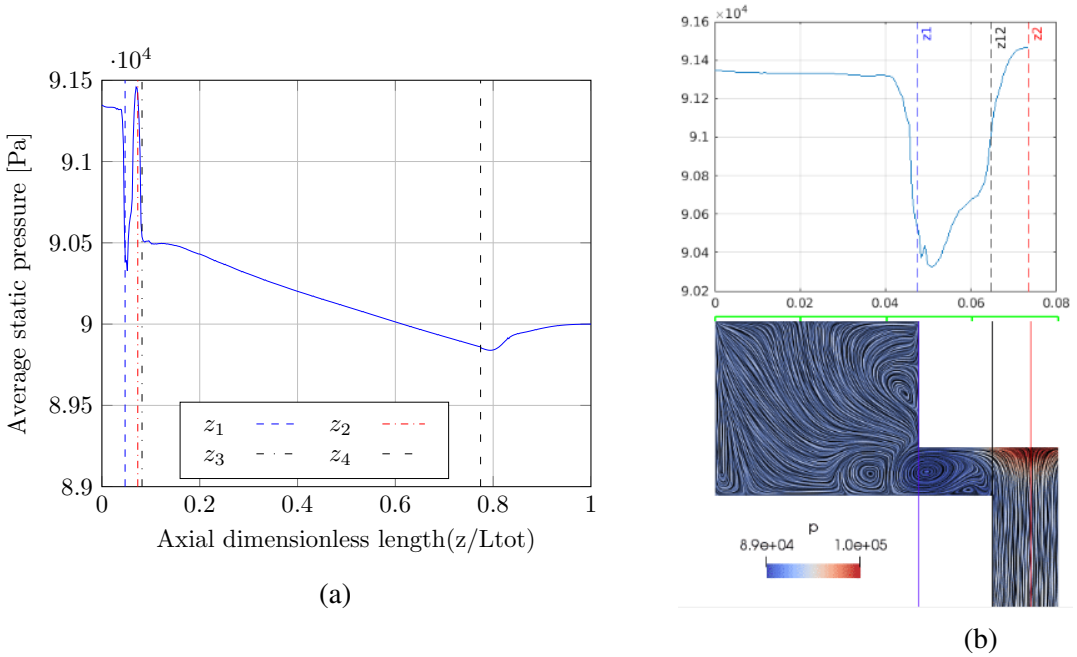

Fig. 4.6 Pressure averaged over section z = constant plotted versus z/L_{tot} - Velocity streamlines and average pressure in front chamber and jet region (b)

The flow entering the front chamber slows down until it almost stops and the pressure stabilizes at a uniform value. In the annular region, except for the first part where the flow is

still affected by the vortices associated with the jet, the transverse velocity components (U_x, U_y) tend to zero, while axial velocity component (U_z) increases and become predominant (see Figure 4.7). The flow accelerates in the axial direction: due to the pressure drops in the annulus, density falls sufficient quickly so that fluid velocity must rise to maintain a constant mass flow rate. The lower the outlet pressure value (p_2), the greater density fall in annular region and as a consequence, the higher the increase of velocity in axial direction (see Figure 4.8).

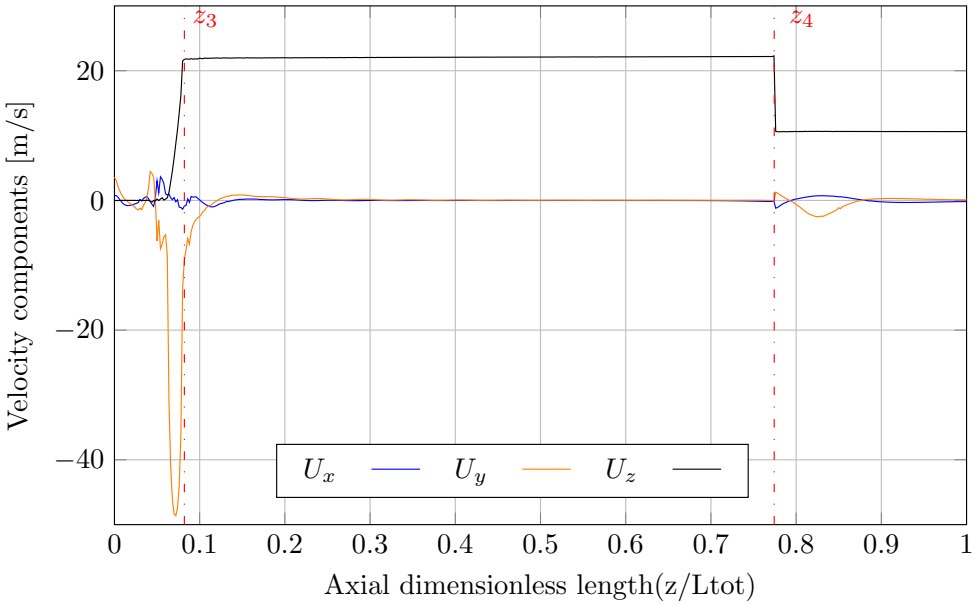

Fig. 4.7 Velocity components averaged over section z = constant plotted versus z/L_{tot} [d = 0.77 mm - L = 32.2 mm - D = 3.6 mm - p_2 = 90 kPa]

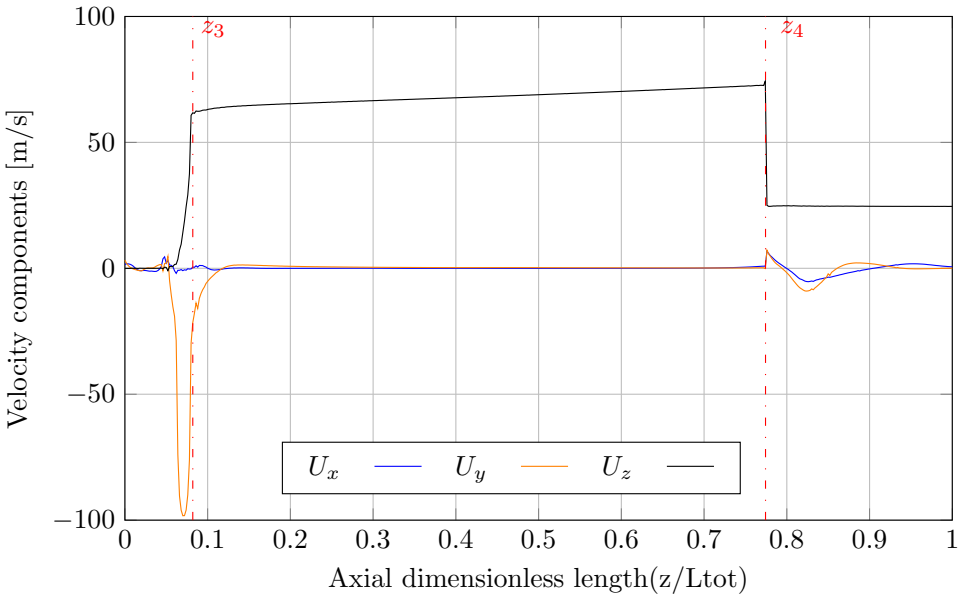

Fig. 4.8 Velocity components averaged over section z = constant plotted versus z/L_{tot} [d = 0.77 mm - L = 32.2 mm - D = 3.2 mm - p_2 = 70 kPa]

The flow at the end of the annulus region (z_4) detaches creating a recirculation bubble whose length increases for lower outlet pressure. Moreover, a secondary recirculation region can be recognized close to the lateral wall due to the adverse pressure gradient occurring in the downstream region. In fact, the lowest pressure is localized just after the base of the releasing mass (see Figure 4.9), and a zone of diffusion is required to recover the outlet pressure. Due to the abrupt increase in the cross section area, occurring passing from the annular to the terminal region, the velocity decreases and a pressure regain occurs.

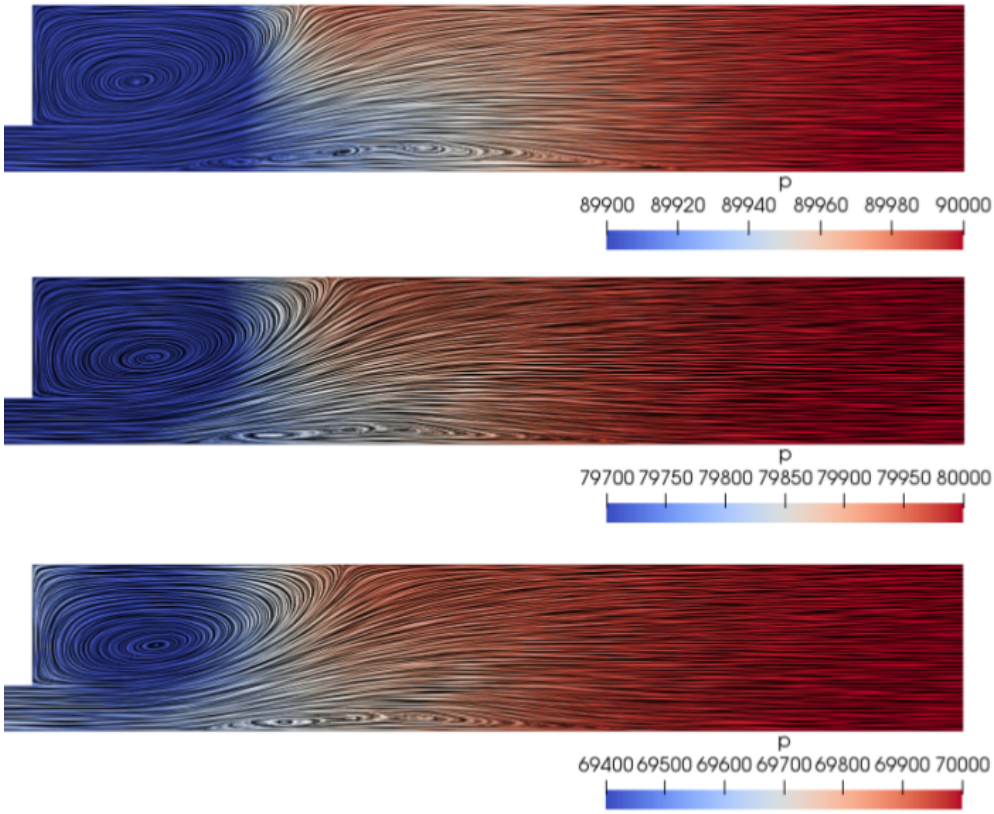

Fig. 4.9 Velocity streamlines and pressure contours in the gripper terminal region at different outlet pressures (d = 0.77 mm - L = 32.2 mm - D = 3.6 mm)

4.3.2 Discussion

The purpose of this section is to illustrate the effect of the parameters (d, L, D, p_2) on the values of mass flow rate ($\dot{m}$) and total force on the releasing mass (F_M).
For a fixed geometry, decreasing outlet pressure (p_2) generates an increment of $\dot{m}$ and F_M (see Figure 4.10). The increment of F_M can be ascribed to both pressure and viscous components. Indeed, decreasing the outlet pressure, a lower pressure is expected also at the base of the releasing mass (near the outflow). Moreover the viscous component increases due to the higher shear stress acting on the releasing mass lateral surface.

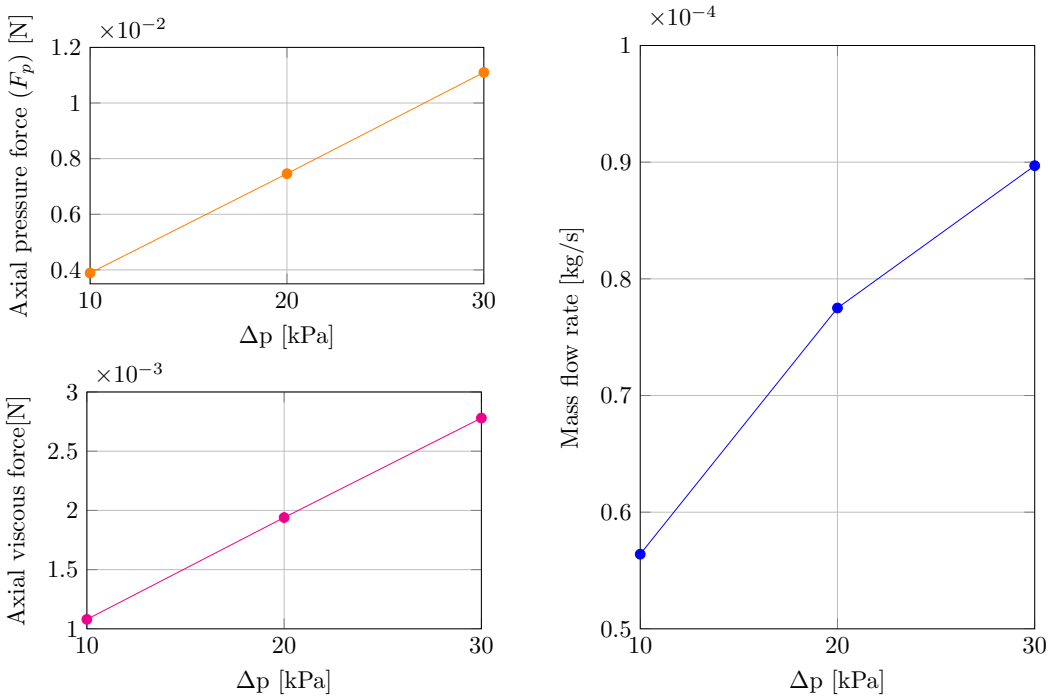

Fig. 4.10 Dependence on imposed negative pressure: axial pressure force (top left), viscous force (bottom left) and mass flow rate (right).

For a fixed outlet pressure, increasing the lateral hole diameter (d) provides higher mass flow rate ($\dot{m}$) and lifting force (F_M) on the releasing mass. The value of L slightly affects mass flow rate, while it influences the viscous part of the lifting force. It is interesting to note how the lifting force (F_M) is strongly related to D value (see Figure 4.11a- 4.11b). A larger annulus area reduces shear stress on the lateral surface and consequentially viscous force (F_V) acting on the releasing mass wall decreases.

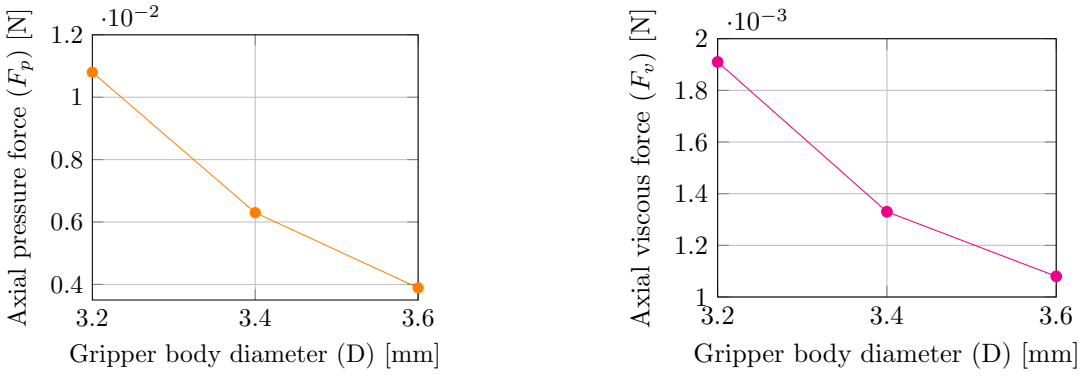

Fig. 4.11 Dependence on gripper body diameter (D): (a) Axial pressure force; (b) Axial viscous force

Similarly, pressure force (F_P) increases as D decreases. Since the pressure force acting on the releasing mass is related to the pressure difference acting on its two bases (p_{sx} and p_{dx}), a possible explanation for F_P trend, can be found out by looking at the pressure drop in the different regions of the gripper. As can be seen from Figure 4.12, the pressure in the front chamber is approximately constant and equal to the pressure acting on the upstream releasing mass base (p_{sx}). Considering Figure 4.12 which plots average static pressure on cross sections versus dimensionless axial direction (z/L_{tot}) the pressure difference acting on the releasing mass ($p_{sx} - p_{dx}$) can be written as:

$$p_{sx} - p_{dx} = \Delta p_j + \Delta p_{AN} \tag{4.3}$$

Where $\Delta p_j = p_{sx} - p(z_3)$ is the pressure difference between the front chamber and the end of the jet region and Δp_{AN} is the pressure difference in the annular region.

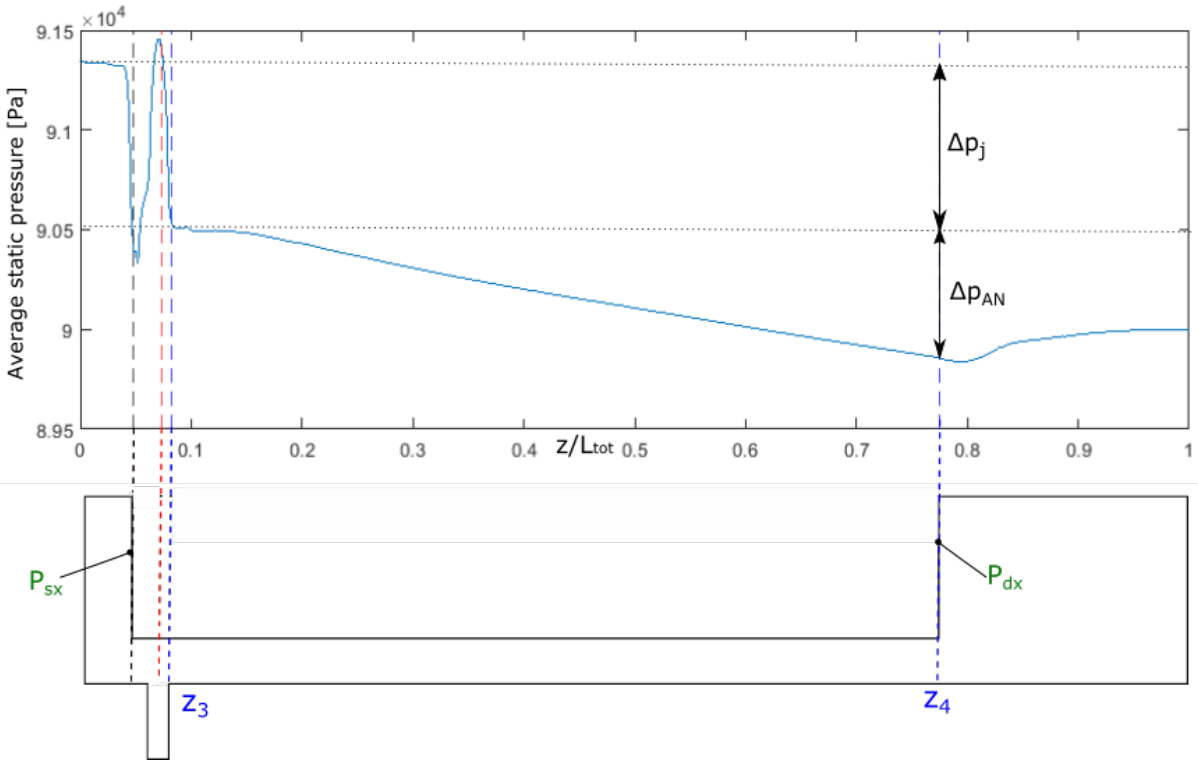

Fig. 4.12 Average static pressure along axial direction

The pressure drop (Δp_j) is controlled by the lateral impinging jet: when the distance between the releasing mass surface and the lateral inlet is smaller, as it happens for smaller D value, the distribution of the mean static pressure on the impinging surface, which has

typically a Gaussian shape, exhibits higher peak pressure. As a result, higher pressure drop is expected between the front chamber and the end of the jet region. Despite the mass flow rate decreases for decreasing D, the pressure drop in the annulus region increases as shown in Figure 4.13.

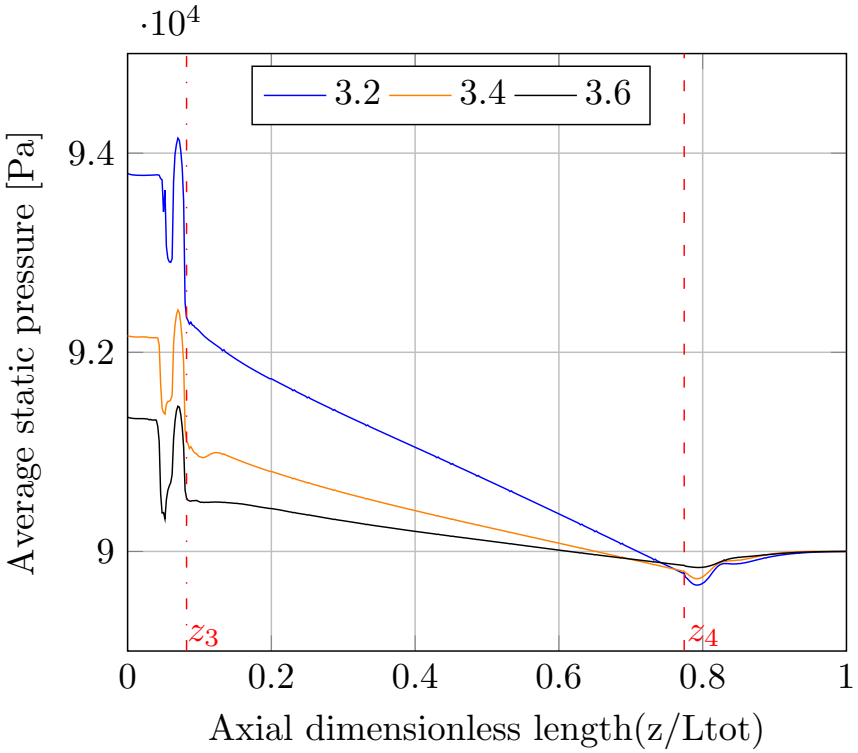

Fig. 4.13 Average static pressure on axial direction at different D values (d = 0.77 mm - L = 32.2 mm).

This behaviour can be justified as follows. Assuming that the flow in the annulus can be approximated as one-dimensional (average axial velocity u_z is dominant), the momentum conservation equation reads:

$$\dot{m}\, du_z = -A_{AN} dp - \tau_w P dz \tag{4.4}$$

Where $A_{AN} = \pi \frac{D^2 - D_1{}^2}{4}$ is the cross section area, $P = \pi(D + D_1)$ the wetted perimeter and τ_w is the wall shear stress in the annulus region. By further rearranging equation 4.4 results in:

$$\frac{dp}{dz} = -\frac{\dot{m}}{A_{AN}} \frac{du_z}{dz} - \frac{4\tau_w}{D - D_1} \tag{4.5}$$

Since $\dot{m} = \rho u_z A_{AN}$ is uniform along the annulus it holds true

$$\rho \frac{du_z}{dz} = -\frac{\dot{m}}{A_{AN}} \frac{1}{\rho} \frac{d\rho}{dz} \tag{4.6}$$

whereas the order of magnitude of the shear stress τ_w can be estimated as

$$\tau_w = \mu \frac{u_z}{D - D_1} = \nu \frac{\dot{m}}{A_{AN}(D - D_1)} \tag{4.7}$$

Equation 4.5 can be rewritten as

$$\frac{dp}{dz} = \left(\frac{\dot{m}}{\rho A_{AN}} \right)^2 \frac{d\rho}{dz} - 4\nu \frac{\dot{m}}{A_{AN}(D - D_1)^2} \tag{4.8}$$

Equation 4.8 integrated along the annular region, yields the pressure drop in the annulus (Δp_{AN})

$$\int_{z_3}^{z_4} \frac{dp}{dz} dz \tag{4.9}$$

Since $\dot{m}$ depends almost linearly on D as it will be shown in section 4.3.3 underneath, and the area of the annulus A_{AN} is proportional to the square of D, the ratio $\frac{\dot{m}}{A_{AN}}$ increases as D decreases. Therefore both terms on the right hand of Equation 4.8 increase for decreasing D.

4.3.3 Empirical correlations

A power law model was chosen to express the dependence of mass flow rate ($\dot{m}$), pressure force (F_P) and viscous force (F_V) on the geometrical factors (d, L, D) and the prescribed pressure (Δp):

$$f = A \prod_j {x_j}^{\alpha j} + \varepsilon \tag{4.10}$$

where f is the dependent variable we want to model (often called response), x_j are the independent variables (often-called predictors), α_j are the model exponents and ε is the model error. Log transforming both sides of equation 4.10, it is possible to obtain a linear form (Equation 4.11) that can be studied using a multiple linear regression approach.

$$\log f = \log A + \sum_j \alpha_j x_j + \log \varepsilon \tag{4.11}$$

$$= \alpha_0 + \sum_i \alpha_j x_j + \widetilde{\varepsilon} \tag{4.12}$$

According to equation 4.12, the following three power law models were assumed:

$$\log\dot{m} = a_0\, d + a_1\, L + a_2\, D + a_3\, \Delta p + \widetilde{\varepsilon_{\dot{m}}}, \tag{4.13}$$

$$\log F_P = b_0\, d + b_1\, L + b_2\, D + b_3\, \Delta p + \widetilde{\varepsilon_{F_P}}, \tag{4.14}$$

$$\log F_V = c_0\, d + c_1\, L + c_2\, D + c_3\, \Delta p + \widetilde{\varepsilon_{F_V}} \tag{4.15}$$

Instead of searching only one correlation for the aerodynamic force F_M, pressure and viscous force values were model separately. The reason for this choice is to be found in the fact that F_P and F_V are related to distinct physical phenomena and it seems therefore more opportune to search for distinct correlations.
For each response, the ordinary Least Square Method (OLS) [27] was applied to identify the appropriate value of the model coefficients (a_j, b_j, c_j) that minimize the model error ($\widetilde{\varepsilon}$). Moreover, a significance analysis was performed to identify variables that are not statistically relevant to predict the response. For this purpose, a statistical hypothesis test has been used:

$$H_0 : \ \alpha_j = 0 \tag{4.16}$$

The null hypothesis (H_0) means that the generic model coefficient α_j is equal to zero and the associated variable x_j does not affect the response. However, even if a variable x_j has no influence on the response (null hypothesis is true), there is a probability, expressed by the p-value, that OLS method applied to the available sample data provides a coefficient α_j significantly higher than zero. So the smaller the p-value, the stronger the evidence that the associate variable represents a meaningful addition to the model.
A backward elimination approach [27] was employed to define the model. It starts from all potential predictors in the regression model and at each step removes the predictor with higher p-value, if greater than the chosen significance level, set to 0.05 [28]. This continues until all variables left in the model are significant.
The following empirical correlations were identified:

$$\dot{m} = 9.88 \times 10^{-6} (d)^{1.9578} (L)^{-0.0141} (D)^{1.0428} (\Delta p)^{0.4371}, \tag{4.17}$$

$$F_P = 114.27\ (d)^{3.1780} (L)^{0.3896} (D)^{-10.21} (\Delta p)^{0.9545}, \tag{4.18}$$

$$F_V = 3.85 \times 10^{-2}\ (d)^{2.3213} (L)^{0.5931} (D)^{-5.52} (\Delta p)^{0.8655}. \tag{4.19}$$

Table 4.3, 4.4 and 4.5 show the output of the significance analysis that has been used to define the empirical correlations.

Table 4.3 Model coefficient and significance analysis: Mass flow rate

Associated variable	p - value	Model coefficients
Intercept	$<$ 2e-16	9.88×10^{-6}
d	$<$ 2e-16	1.9578
L	0.00454	-0.0141
D	$<$ 2e-16	1.0428
Δp	$<$ 2e-16	0.4371

Table 4.4 Model coefficient and significance analysis:Pressure force

Associated variable	p - value	Model coefficients
Intercept	<2e-16	114.27
d	<2e-16	3.1780
L	<2e-16	0.3896
D	<2e-16	-10.2100
Δp	<2e-16	0.9545

Table 4.5 Model coefficient and significance analysis:Viscous force

Associated variable	p - value	Model coefficients
Intercept	<2e-16	3.85×10^{-2}
d	<2e-16	2.3213
L	<2e-16	0.5931
D	<2e-16	-5.5231
Δp	<2e-16	0.8655

Figures 4.14, 4.15 and 4.16 show the mass flow rate ($\dot{m}$), the pressure force (F_P) and the viscous force (F_V) predicted by CFD simulations and the empirical model. All models achieve a good agreement with CFD data with an average error below 10% for the mass flow rate and 11% for force values.

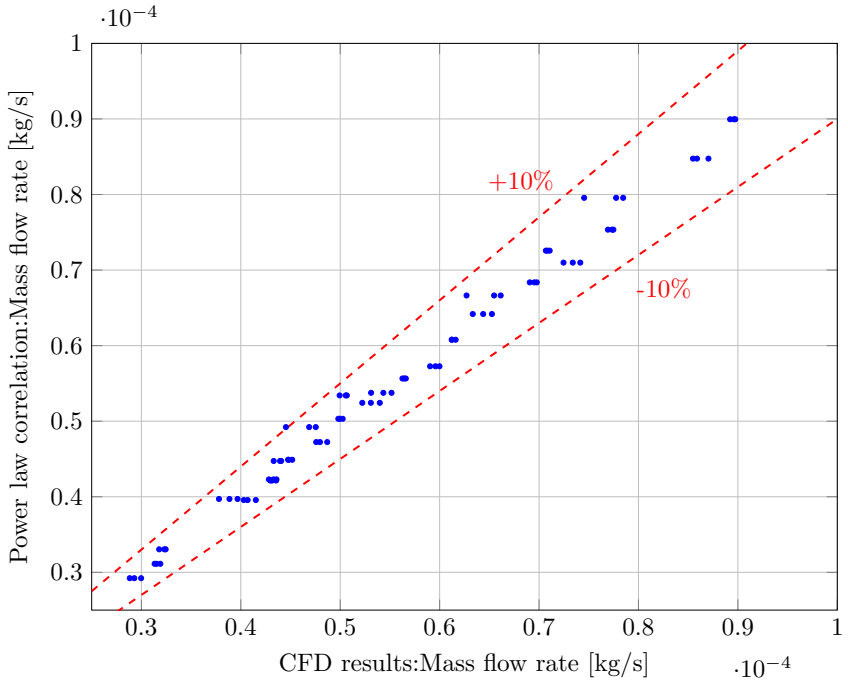

Fig. 4.14 Mass flow rate empirical model: CFD simulation versus empirical model predicted value

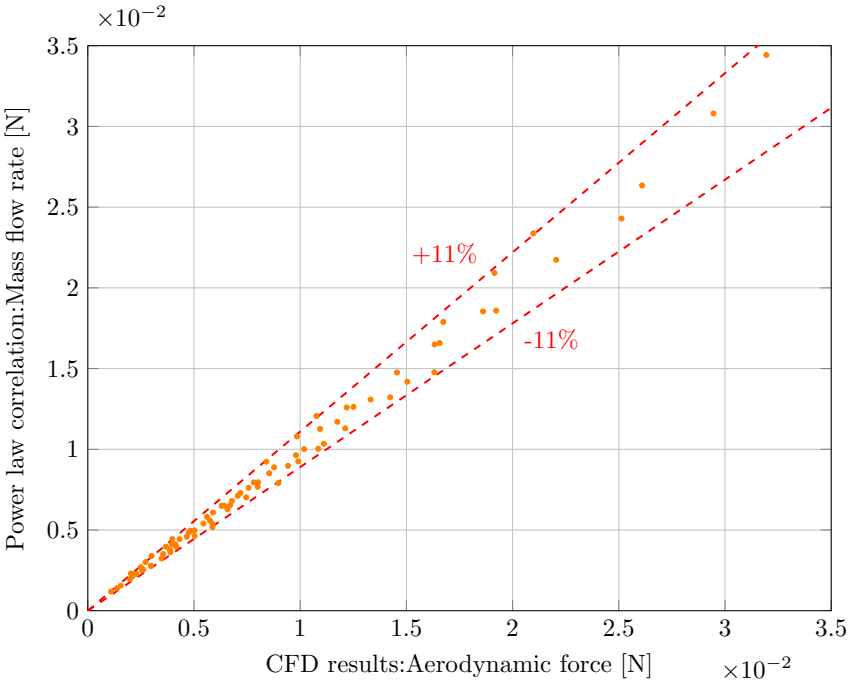

Fig. 4.15 Pressure force empirical model: CFD simulation versus empirical model predicted value

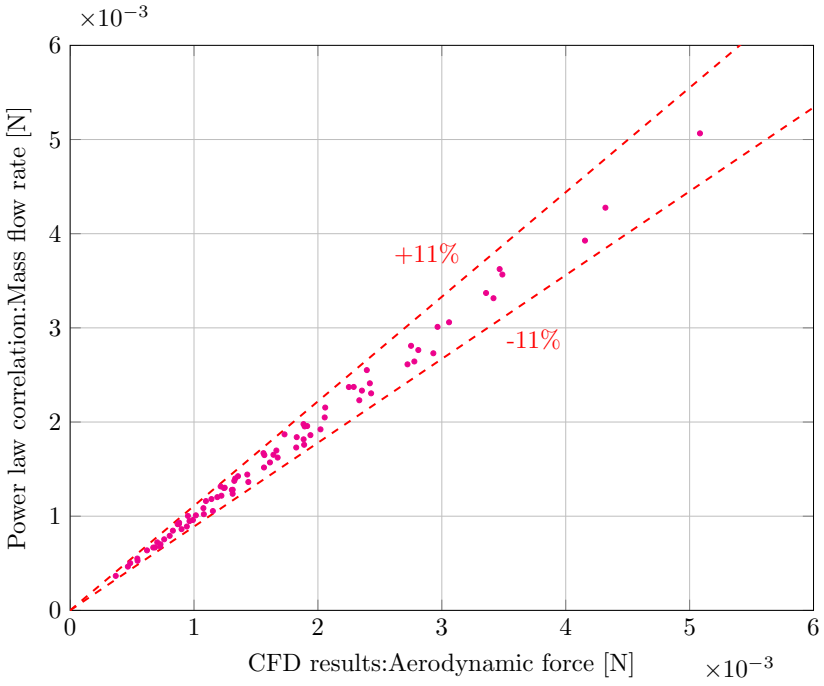

Fig. 4.16 Viscous force empirical model: CFD simulation versus empirical model predicted value

Conclusions

In this thesis the fluid dynamics of a vacuum microgripper with an integrated releasing tool was numerically investigated.
The research aimed to analyse how the geometry of the device and the value of the imposed Δp influence the mass flow rate ($\dot{m}$) inside the gripper and the aerodynamic force (F_M) on the releasing tool to provide helpful information for the design process. A complete CFD analysis was performed to investigate the fluid dynamics of 27 different geometrical configurations, varying the value of three geometrical parameters (d, L, D). For each geometry computation was performed for three different values of the outlet pressure (p_2 = 90 - 80 - 70 kPa). Significant efforts were made to define a computational model suitable for this type of analysis.
Two aspects, in particular, have been taken into account:

- the robustness of the model in order to get rid of the convergence and stability problems that emerged in a first part of the study
- capability of providing satisfactory data, limiting the overall calculation time, a variable of no small importance given the number of simulations to be carried out (i.e. 81).

The RANS approach proved to be the best way of meeting these two requirements. In the thesis, it has been shown that, by taking the LES results as a reference, the RANS approach can provide sufficiently accurate results, in terms of $\dot{m}$ and F_M, if one chooses a suitable mesh resolution, especially in the wall region. Furthermore, while being aware of its limited accuracy in predicting the absolute value of $\dot{m}$ and F_M, the final RANS approach adopted with coarse grids (G4) can estimate the order of magnitude of both quantities within a reasonable computation time. Indeed, RANS simulation on a finer grid (G3) for one case demonstrated that computation time would be too long to perform all 81 simulations.
Correlations based on a power-law model for predicting mass flow rate ($\dot{m}$), pressure (F_P) and viscous force (F_V) upon varying d, L, D and Δp are proposed in Chapter 4. Data of $\dot{m}$, F_P and F_V obtained from all 81 CFD simulations are used to generate data source for regressing

the correlations' coefficients using the OLS method. P-value was used to test the statistical significance of each variables (d, L, D, Δp).

The numerical correlations agree with the simulations data and show acceptable errors (less than 11%). Of course, these correlations are strictly representative of the device taken into account and have no general validity. Moreover, the power-law correlations adopted are pretty simple and cannot describe, for example, non-monotonic dependencies on the variables, although they are effective for a limited range of value of the four factors such as those investigated in this study. Despite these limitations, this study provided further evidence that the approach applied is valid and the application under consideration has shown its applicability to an industrial case. The correlations proposed here represent a valuable tool to speed up the micro-gripper design, carrying out initial estimate of F_M for a preliminary design.
The study also highlighted some characteristics of the flow field.

- The 3D streamlines analysis obtained from LES computation results showed that the flow in the front chamber is not stagnant: air does circulate at low velocities. This observation stressed the importance of guarantee a sufficiently high mesh resolution also in the front chamber region, contrary to what was expected.

- The lateral impinging jet seems to influence the pressure in the front chamber significantly. The analysis of CFD results indicates that the closer is the distance between the jet and the impinged wall, the higher is the pressure in the front chamber and the pressure drops in the annular region. Consequentially, the pressure force (F_P) acting on the releasing mass increases. In this light, the value of body inner diameter (D) plays a crucial role in affecting F_M and must be carefully chosen during the design process.

Future studies are recommended in order to elucidate deeply how lateral impinging jet features and front chamber region features can affect the dependency between F_M and D. For example, the lateral jet axial position (l_1) or the distance between the bottom wall and the releasing mass (l_2), kept constant in this study, could be varied.
Moreover, this research could serve as a base for future investigations extending the range of parameters values explored and addressing the study of an improved design of the vacuum micro-gripper optimized to the best.

.

References

[1] Serena Ruggeri, Gianmauro Fontana, Giovanni Legnani, and Irene Fassi. Design strategies for vacuum micro-grippers with integrated release system. In *International Design Engineering Technical Conferences and Computers and Information in Engineering Conference*, volume 58165, page V004T09A022. American Society of Mechanical Engineers, 2017.

[2] Marcel Tichem, Defeng Lang, and Bernhard Karpuschewski. A classification scheme for quantitative analysis of micro-grip principles. *Assembly automation*, 2004.

[3] Gualtiero Fantoni, Marco Santochi, Gino Dini, Kirsten Tracht, Bernd Scholz-Reiter, Juergen Fleischer, Terje Kristoffer Lien, Guenther Seliger, Gunther Reinhart, Joerg Franke, et al. Grasping devices and methods in automated production processes. *CIRP Annals*, 63(2):679–701, 2014.

[4] Hui Xie, Xianghe Meng, Hao Zhang, and Lining Sun. Development of a magnetically driven microgripper for piconewton force-controlled microscale manipulation and characterization. *IEEE Transactions on Industrial Electronics*, 67(3):2065–2075, 2019.

[5] Chen Wenjie and Lin Wei. Design of a flexure-based gripper used in optical fiber handling. In *IEEE Conference on Robotics, Automation and Mechatronics, 2004.*, volume 1, pages 83–88. IEEE, 2004.

[6] Wolfgang Zesch, Markus Brunner, and Ariel Weber. Vacuum tool for handling microobjects with a nanorobot. In *Proceedings of International Conference on Robotics and Automation*, volume 2, pages 1761–1766. IEEE, 1997.

[7] Stefano Oberti, Adrian Neild, Dirk Möller, and Jürg Dual. Towards the automation of micron-sized particle handling by use of acoustic manipulation assisted by microfluidics. *Ultrasonics*, 48(6-7):529–536, 2008.

[8] Jing Liu, Yi-Xin Zhou, and Tian-Hua Yu. Freeze tweezer to manipulate mini/micro objects. *Journal of Micromechanics and Microengineering*, 14(2):269, 2003.

[9] Pierre Lambert. *Capillary forces in microassembly: modeling, simulation, experiments, and case study*. Springer Science & Business Media, 2007.

[10] Ronald S Fearing. Survey of sticking effects for micro parts handling. In *Proceedings 1995 IEEE/RSJ International Conference on Intelligent Robots and Systems. Human Robot Interaction and Cooperative Robots*, volume 2, pages 212–217. IEEE, 1995.

[11] Gualtiero Fantoni and Marcello Porta. A critical review of releasing strategies in microparts handling. In *International Precision Assembly Seminar*, pages 223–234. Springer, 2008.

[12] Weibin Rong, Zenghua Fan, Lefeng Wang, Hui Xie, and Lining Sun. A vacuum microgripping tool with integrated vibration releasing capability. *Review of Scientific Instruments*, 85(8):085002, 2014.

[13] Dragan Petrovic, Gordana Popovic, Elias Chatzitheodoridis, Oscar Del Medico, Ana Almansa, F Sumecz, Werner Brenner, and Helmut Detter. Gripping tools for handling and assembly of microcomponents. In *2002 23rd International Conference on Microelectronics. Proceedings (Cat. No. 02TH8595)*, volume 1, pages 247–250. IEEE, 2002.

[14] Mélanie Dafflon, Benoit Lorent, and Reymond Clavel. A micromanipulation setup for comparative tests of microgrippers. In *International Symposium on Robotics*, number CONF, 2006.

[15] Gianmauro Fontana, Serena Ruggeri, Giovanni Legnani, and Irene Fassi. Precision handling of electronic components for pcb rework. In *International Precision Assembly Seminar*, pages 52–60. Springer, 2014.

[16] Alessandro Morelli. Modellazione e simulazione numerica di deflussi in microdispositivi di presa ad aspirazione. Master's thesis, Università degli studi di Brescia, a.a 2015-2016.

[17] Serena Ruggeri, Gianmauro Fontana, Antonio Ghidoni, Alessandro Morelli, Giovanni Legnani, Adriano Maria Lezzi, and Irene Fassi. A preliminary fluid dynamic model of a vacuum micro-gripper with integrated release system. In *ASME 2018 International Design Engineering Technical Conferences and Computers and Information in Engineering Conference*. American Society of Mechanical Engineers Digital Collection.

[18] Gianmauro Fontana, Serena Ruggeri, Antonio Ghidoni, Alessandro Morelli, Giovanni Legnani, Adriano Maria Lezzi, and Irene Fassi. Fluid dynamics aided design of an innovative micro-gripper. In *International Precision Assembly Seminar*, pages 214–225. Springer, 2018.

[19] OpenFOAM 4.1,https://openfoam.org, 13 Oct. 2016.

[20] Ronald Aylmer Fisher et al. The design of experiments. *The design of experiments.*, (2nd Ed), 1937.

[21] Timothy A Cleaver, Alex J Gutman, Christopher L Martin, Mark F Reeder, and Raymond R Hill. Using design of experiments methods for applied computational fluid dynamics: A case study. *Quality Engineering*, 28(3):280–292, 2016.

[22] Rajdip Paul and Sujit Dalui. Shape optimization to reduce wind pressure on the surfaces of a rectangular building with horizontal limbs. *Periodica Polytechnica Civil Engineering*, 65(1):134–149, 2021.

[23] Vinod Kumar Srinivasa, S Renjith, and Biswadip Shome. Design of experiments enabled cfd approach for optimizing cooling fan performance. Technical report, SAE Technical Paper, 2014.

[24] Python Language Reference, version 3.0, http://www.python.org.

[25] R Core Team. *R: A Language and Environment for Statistical Computing*. R Foundation for Statistical Computing, Vienna, Austria, 2013.

[26] Akira Yoshizawa. Statistical theory for compressible turbulent shear flows, with the application to subgrid modeling. *The Physics of fluids*, 29(7):2152–2164, 1986.

[27] Norman R Draper and Harry Smith. *Applied regression analysis*, volume 326. John Wiley & Sons, 1998.

[28] Jae H Kim and In Choi. Choosing the level of significance: A decision-theoretic approach. *Abacus*, 57(1):27–71, 2021.

Appendix A

Rapidograph technical draw

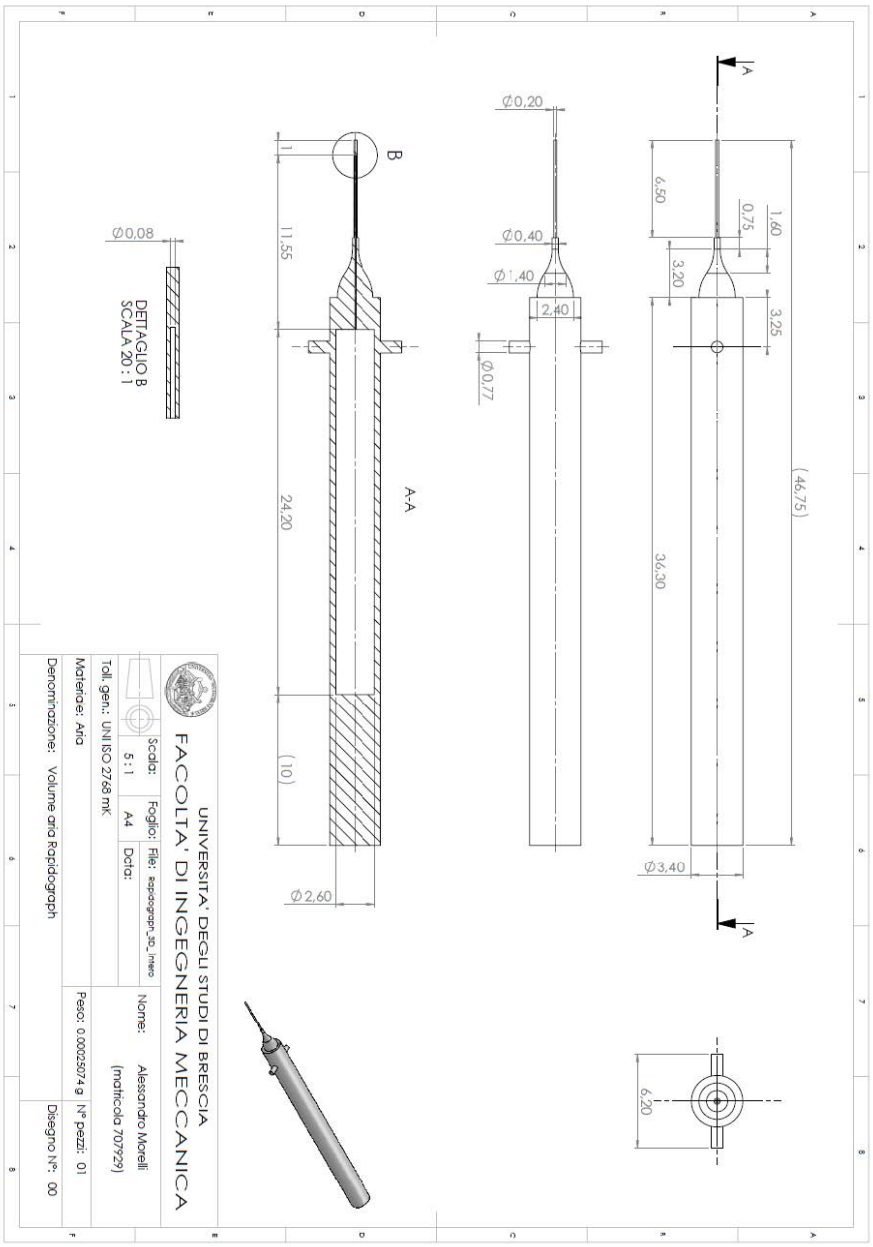

Appendix B

Preliminary CFD study

This section presents the results obtained from the first CFD analysis performed on the investigated vacuum microgripper and described in a Master Thesis [16]. The results obtained and the limitations of this first analysis have constituted the starting point and the stimulus for further in-depth studies carried out during my Ph.D.
The computational domain is sketched in Figure B.1.

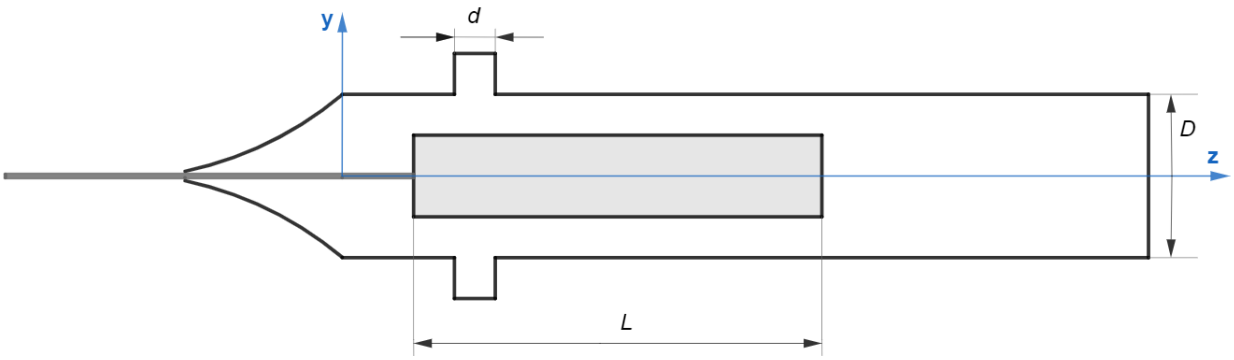

Fig. B.1 Computational domain used in preliminar CFD study

To understand how internal flow fields could be affected by the imposed pressure drop (Δp), three different simulations were carried out, imposing three different values of static pressure at the outlet section (p_2 = 90 - 80 - 70 kPa).

Taking advantage of the symmetry of the problem with respect to the xz-plane, the simulation was conducted only on half of the volume of the entire device, imposing a symmetry boundary condition along the symmetry plane. A classical RANS approach is chosen for the analysis, using a stationary compressible solver (*rhoSimpleFoam*), combined with a turbulence model (k-ω *SST*), without the aid of wall functions.

The computational grid used to discretize the computational domain was chosen downstream of a grid independence study to identify the optimal grid resolution. The chosen mesh consists of 0.473×10^6 elements (hexahedra and tetrahedra) with cell resolution at the wall such that it has a value of y^+=1.

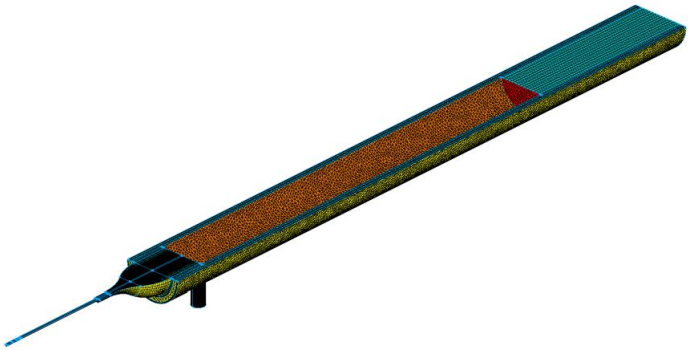

Fig. B.2 Grid of the computational domain

The following figures show the pressure and velocity fields obtained from the simulation at p_2 = 90 kPa.

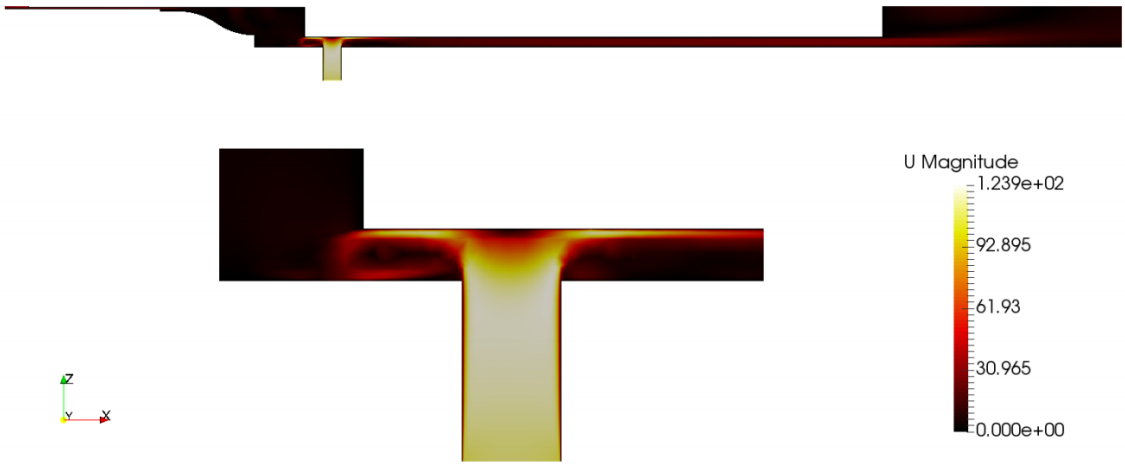

Fig. B.3 Velocity magnitude field at the middle plane - p_2 = 90 kPa

Mass flow rate values at inlet (cannula and lateral holes) and outlet sections are computed as well. Conceptually, the total air mass flow through the device ($\dot{m}_2$) is given by the sum of two contributions: the air flow through the cannula ($\dot{m}_0$) and the incoming air from the lateral holes ($\dot{m}_1$).

$$\dot{m}_2 = \dot{m}_0 + \dot{m}_1 \tag{B.1}$$

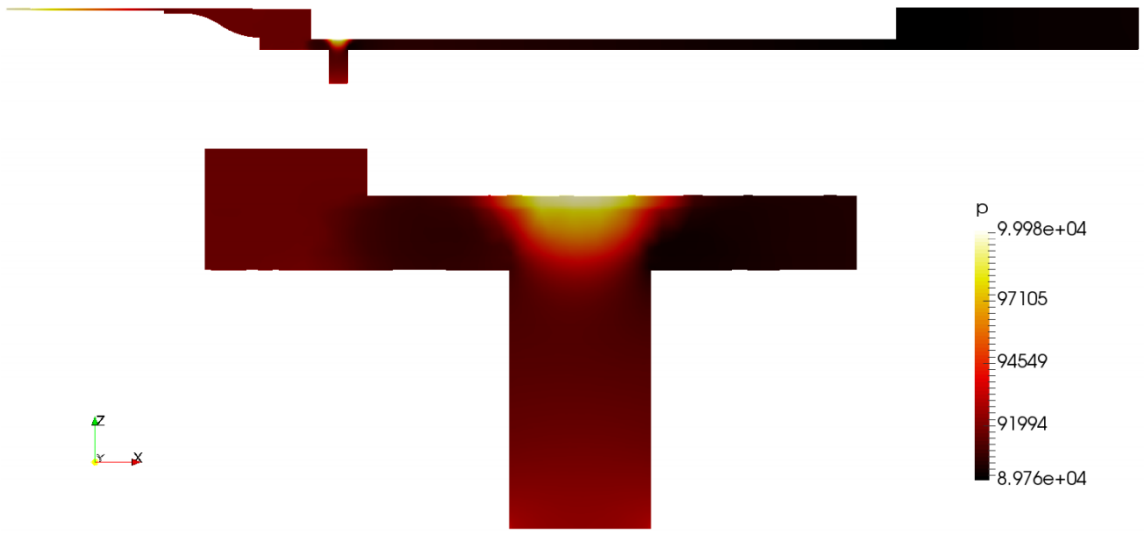

Fig. B.4 Static pressure field at the middle plane - p_2 = 90 kPa

However computed values, illustrated in Table B.1, show that the mass flow rate through the cannula ($\dot{m}_0$) is very small, two orders of magnitude lower, compared to the one through the lateral holes ($\dot{m}_1$). This was reasonable to expect considering that the cannula inner diameter (d_0) is significantly smaller than the lateral holes diameter (d).

Table B.1 CFD computed mass flow rate values

p_2	Mass flow rates [kg/s]		
[kPa]	$\dot{m}_0$	$\dot{m}_1$	$\dot{m}_2$
90	7.12×10^{-7}	1.13×10^{-4}	1.13×10^{-4}
80	1.05×10^{-6}	1.49×10^{-4}	1.48×10^{-4}
70	1.44×10^{-6}	1.75×10^{-4}	1.76×10^{-4}

Since the airflow through the cannula ($\dot{m}_0$) does not significantly affect the total airflow through the device ($\dot{m}_2$), it can be conceivably assumed that flow fields inside the gripper and so fluid-dynamic force acting on the releasing mass are not influenced as well and it is possible to decouple the fluid-dynamic problem, studying separately the cannula and the gripper body (see Figure B.6). To verify the effectiveness of this decoupling approach, two CFD simulations were provided on the cannula and the gripper body separately. The values of mass flow rates at the two inlets and total force on releasing mass were computed and compared with the ones obtained from entire geometry simulation.

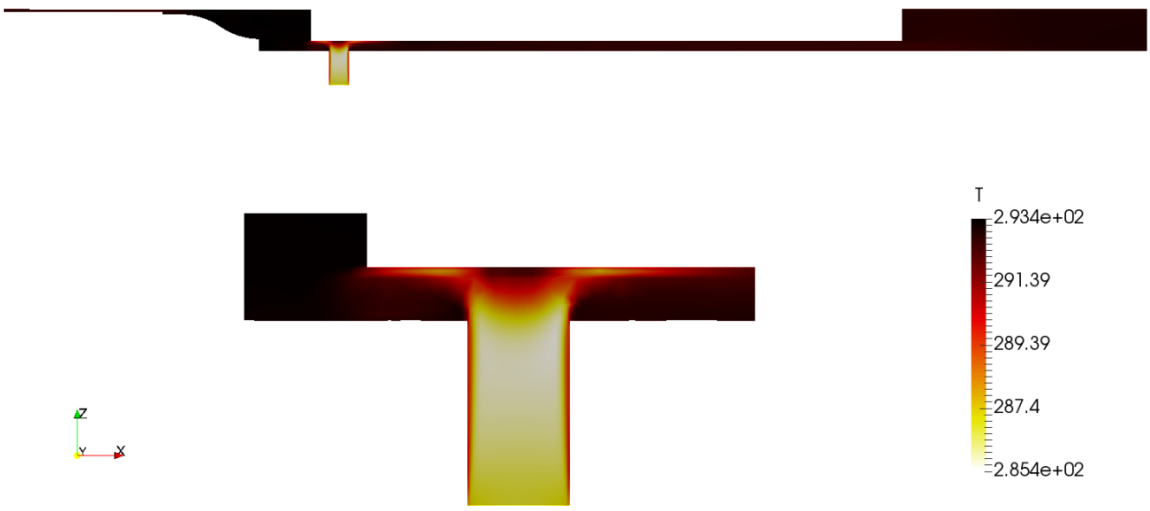

Fig. B.5 Temperature field at the middle plane - p_2=90 kPa

Fig. B.6 Decoupled problems

The value of mass flow rates and total force on the releasing mass obtained considering cannula and gripper body as two separate problems are presented in Table B.2. The comparison with data obtained from simulation on entire geometry shows that the differences obtained in the mass flow calculation are less than 1%, while the difference in the force value in percentage terms is slightly higher and is around 1.04% (see Table B.3).

Table B.2 CFD computed mass flow rates and total force values: Decoupled problems

		$\dot{m}_0$	$\dot{m}_1$	F_M
Decoupled problems	Cannula	7.15×10^{-7}	-	-
	Gripper body	-	1.154×10^{-4}	1.44×10^{-2}
	Cannula + Gripper body	7.15×10^{-7}	1.154×10^{-4}	1.44×10^{-2}

Table B.3 Comparison between ecoupled problems and entire geometry results

	$\dot{m}_0$	$\dot{m}_1$	F_M
Cannula + Gripper body	7.15×10^{-7}	1.154×10^{-4}	1.44×10^{-2}
Entire geometry	7.14×10^{-7}	1.146×10^{-4}	1.455×10^{-2}
Change (%)	0.14 %	0.69 %	1.04 %

Such differences in computed values of $\dot{m}$ and F_M are sufficient to justify a decoupled study of the fluid dynamics of the micro-gripper. Therefore, only the analysis of the gripper body will be adopted in the continuation of the study.

Appendix C

RANS1 study: CFD results and empirical correlations

C.1 Results: $\dot{m}$ and F_M values

Both the value of mass flow rate $\dot{m}$ and F_M are provided by post processing of RANS1 simulation data and are listed in table C.1 and C.2 respectively.

Table C.1 RANS1 CFD results: mass flow rate $\dot{m}$

d	L	D	p_2				
mm	mm	mm	kPa				
			90	85	80	75	70
			Mass flow rate $\times 10^{-5}$ kg/s				
0.59	16.2	3.2	2.62	3.17	3.59	3.97	4.27
0.59	16.2	3.6	2.84	3.42	3.89	4.23	4.51
0.59	24.2	3.4	2.75	3.32	3.75	4.13	4.41
0.59	32.2	3.2	2.63	3.17	3.54	3.93	4.22
0.59	32.2	3.6	2.82	3.40	3.84	4.22	4.50
0.69	16.2	3.6	4.08	4.90	5.57	6.06	6.45
0.69	24.2	3.4	3.92	4.73	5.36	5.90	6.30
0.69	32.2	3.6	4.00	4.82	5.47	6.01	6.42
0.77	16.2	3.2	4.41	5.35	6.13	6.71	7.22

Table C.1 RANS1 CFD results: mass flow rate $\dot{m}$

d	L	D	p_2				
mm	mm	mm	kPa				
			90	85	80	75	70
			Mass flow rate $\times 10^{-5}$ kg/s				
0.77	16.2	3.6	5.13	6.22	6.99	7.67	8.19
0.77	24.2	3.2	4.36	5.33	6.01	6.61	7.14
0.77	24.2	3.4	4.92	5.95	6.74	7.41	7.91
0.77	24.2	3.6	5.11	6.16	7.00	7.65	8.18
0.77	32.2	3.2	4.37	5.33	6.06	6.65	7.19
0.77	32.2	3.6	5.13	-	7.00	-	8.18

Table C.2 RANS1 CFD results: aerodynamic force F_M

d	L	D	p_2				
mm	mm	mm	kPa				
			90	85	80	75	70
			Aerodynamic force $\times 10^{-3}$ N				
0.59	16.2	3.2	3.70	5.04	6.52	8.15	9.91
0.59	16.2	3.6	1.05	1.40	1.84	2.21	2.60
0.59	24.2	3.4	2.90	3.92	4.93	6.11	7.27
0.59	32.2	3.2	3.66	5.33	7.95	10.6	13.1
0.59	32.2	3.6	1.79	2.41	2.86	3.57	4.21
0.69	16.2	3.6	1.94	2.73	3.52	4.78	5.69
0.69	24.2	3.4	4.25	5.92	7.57	9.62	11.5
0.69	32.2	3.6	2.94	4.01	5.22	6.67	8.02
0.77	16.2	3.2	8.47	11.8	16.1	20.1	24.2
0.77	16.2	3.6	3.07	4.45	5.64	7.34	8.32
0.77	24.2	3.2	10.2	16.0	19.6	24.3	29.2

Table C.2 RANS1 CFD results: aerodynamic force F_M

d	L	D	p_2				
mm	mm	mm	kPa				
			90	85	80	75	70
			Aerodynamic force $\times 10^{-3}$ N				
0.77	24.2	3.4	6.74	9.53	12.3	15.2	18.2
0.77	24.2	3.6	3.84	5.23	6.84	8.24	9.98
0.77	32.2	3.2	11.2	16.4	21.8	26.6	32.4
0.77	32.2	3.6	3.89	-	6.89	-	9.76

C.2 Empirical correlations

The results obtained from the first CFD analysis (RANS1) were used to determine analytical correlations capable of predicting with sufficient accuracy the value of $\dot{m}$ and F_M, given the geometry of the device (d,L,D) and the value of the pressure imposed at the outlet (p_2). The OLS method was implemented with the help of R software [25] on all 45 simulations carried out. A different correlation was investigated separately for pressure (F_P) and viscous (F_V) force, rather than considering the total aerodynamic force (F_M). For both the prediction of $\dot{m}$, F_P and F_V, a power law was assumed as a correlation. The power law correlation was log-transformed in order to used the OLS method.

$$\log\dot{m} = a_0\, d + a_1\, L + a_2\, D + a_3\, \Delta p + \widetilde{\varepsilon_{\dot{m}}}, \tag{C.1}$$

$$\log F_P = b_0\, d + b_1\, L + b_2\, D + b_3\, \Delta p + \widetilde{\varepsilon_{F_P}}, \tag{C.2}$$

$$\log F_V = c_0\, d + c_1\, L + c_2\, D + c_3\, \Delta p + \widetilde{\varepsilon_{F_V}} \tag{C.3}$$

OLS method was applied to mass flow rate values and firstly all variables (d,L,D,Δp) were taken into account. Variable coefficients and associated p-value are summarized in Table C.3 The p-value associated to L suggested that, according to data set analyzed, the releasing mass length (L) does not affect mass flow rate ($\dot{m}$). As a consequence, the OLS method was applied again, removing L from the calculus. New value coefficients for mass flow rate are summarized in Table C.4.

Table C.3 Model coefficient and significance analysis: Mass flow rate

Associated variable	p - value	Model coefficients
Intercept	$< 2 \times 10^{-16}$	9.695×10^{-6}
d	$< 2 \times 10^{-16}$	2.1067
L	0.274	-0.0103
D	$< 2 \times 10^{-16}$	0.9701
Δp	$< 2 \times 10^{-16}$	0.4339

Table C.4 Model coefficient and significance analysis: Mass flow rate

Associated variable	p - value	Model coefficients
Intercept	$< 2 \times 10^{-16}$	9.3773×10^{-6}
d	$< 2 \times 10^{-16}$	2.1069
D	$< 2 \times 10^{-16}$	0.9722
Δp	$< 2 \times 10^{-16}$	0.4340

The correlation found for mass flow rate shows a good agreement with CFD data with an error below 5% as shown in Figure C.1

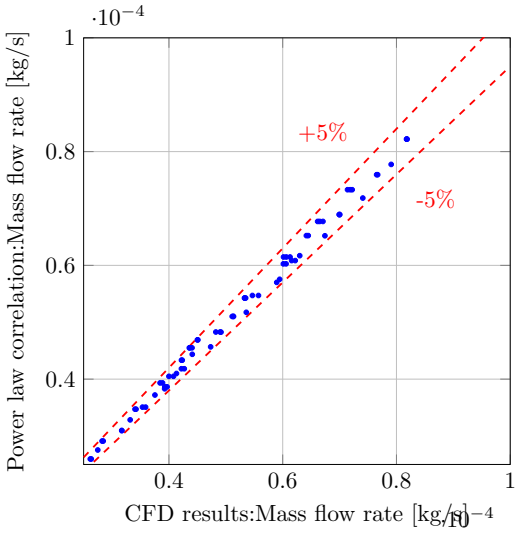

Fig. C.1 Mass flow rate empirical model: CFD simulation versus empirical model predicted value

The same approach was applied to F_P and F_V data and similar correlations was found. Tables C.5 and C.6 report correlations' coefficients for F_P and F_v respectively, while Figure C.2 shows error on the aerodynamic force F_M.

Table C.5 Model coefficient and significance analysis: Pressure force F_P

Associated variable	**p - value**	**Model coefficients**
Intercept	$< 1.1 \times 10^{-4}$	42.4756
d	$< 2 \times 10^{-16}$	3.8722
L	$< 8 \times 10^{-4}$	0.4246
D	$< 2 \times 10^{-16}$	-9.5194
Δp	$< 2 \times 10^{-16}$	0.9706

Table C.6 Model coefficient and significance analysis: Viscous force F_V

Associated variable	**p - value**	**Model coefficients**
Intercept	$< 2 \times 10^{-6}$	1.257×10^{-2}
d	$< 2 \times 10^{-16}$	2.5747
D	$< 2 \times 10^{-16}$	-4.8536
L	$< 2 \times 10^{-16}$	0.6633
Δp	$< 2 \times 10^{-16}$	0.8252

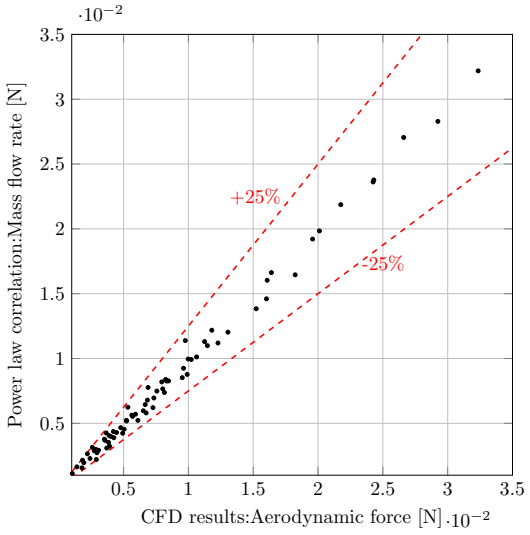

Fig. C.2 Mass flow rate empirical model: CFD simulation versus empirical model predicted value

Appendix D

OpenFOAM settings

D.1 RANS1

```
// ************************************************************************* //
ddtSchemes
{
    default steadyState;;
}
gradSchemes
{
    default cellLimited Gauss linear 1; OR cellLimited leastSquares 1;
    grad(U) cellLimited Gauss linear 1; OR cellLimited leastSquares 1;
}
divSchemes
{
    default none;
    div(phi,U) bounded Gauss skewCorrected linearUpwindV grad(U);
    div(phi,e) bounded Gauss upwind;
    div(phi,epsilon) bounded Gauss upwind;
    div(phi,omega) bounded Gauss upwind;
    div(phi,k) bounded Gauss upwind;
    div(phi,Ekp) bounded Gauss upwind;
    div(((rho*nuEff)*dev2(T(grad(U))))) Gauss linear;
}
laplacianSchemes
{
```

```
    default Gauss linear limited 0.333;
}
interpolationSchemes
{
    default linear;
}
snGradSchemes
{
    default corrected;
}
wallDist
{
    method meshWave;
}
// ************************************************************************* //
```

D.2 LES

```
// ************************************************************************* //
ddtSchemes
{
    default Euler;
}
gradSchemes
{
    default cellMDLimited Gauss linear 1;
}
divSchemes
{
    default none;
    div(phi,U) Gauss limitedLinear 1;
    div(phi,e) Gauss limitedLinear 1;
    div(phi,k) bounded Gauss upwind;
    div(phi,K) Gauss limitedLinear 1;
    div(((rho*nuEff)*dev2(T(grad(U))))) Gauss linear;
    div(phid,p) Gauss limitedLinear 1;
```

```
    div(phiv,p) Gauss limitedLinear 1;
    div(phi,Ekp) Gauss limitedLinear 1;
}
laplacianSchemes
{
    default Gauss linear corrected;
}
interpolationSchemes
{
    default linear;
}
snGradSchemes
{
    default corrected;
}
wallDist
{
    method meshWave;
}
// ************************************************************************* //
```

D.3 RANS4

```
// ************************************************************************* //
ddtSchemes
{
    default Euler;
}
gradSchemes
{
    default Gauss linear;
    grad(U) cellLimited Gauss linear 1;
}
divSchemes
{
    default none;
```

```
    div(phi,U) bounded Gauss linearUpwindV grad(U);
    div(phi,e) bounded Gauss upwind;
    div(phi,omega) bounded Gauss upwind;
    div(phi,k) bounded Gauss upwind;
    div(phi,K) bounded Gauss upwind;
    div(((rho*nuEff)*dev2(T(grad(U))))) Gauss linear;
    div(phiv,p) bounded Gauss upwind;
    div(phi,Ekp) bounded Gauss upwind;
}
laplacianSchemes
{
    default Gauss linear limited 0.5;
}
interpolationSchemes
{
    default linear;
}
snGradSchemes
{
    default limited 0.5;
}
wallDist
{
    method meshWave;
}
// ************************************************************************* //
```

Appendix E

RANS4 study: CFD results

Tables E.1, E.2 and E.3 listed $\dot{m}$, F_P and F_V values carried out by all simulations conducted in RANS4 study.

Table E.1 RANS4 CFD results: mass flow rate $\dot{m}$

d	L	D	p_2		
mm	mm	mm	kPa		
			90	80	70
			Mass flow rate 10^{-5} kg/s		
0.59	16.2	3.2	3.00	4.15	4.87
0.59	16.2	3.4	3.19	4.35	5.02
0.59	16.2	3.6	3.24	4.41	5.07
0.59	24.2	3.2	2.93	4.07	4.80
0.59	24.2	3.4	3.15	4.32	5.00
0.59	24.2	3.6	3.23	4.39	5.05
0.59	32.2	3.2	2.88	4.03	4.76
0.59	32.2	3.4	3.13	4.30	4.98
0.59	32.2	3.6	3.18	4.33	4.99
0.69	16.2	3.2	3.97	5.52	6.53
0.69	16.2	3.4	4.36	6.00	6.98
0.69	16.2	3.6	4.52	6.16	7.11

Table E.1 RANS4 CFD results: mass flow rate $\dot{m}$

d	L	D	p_2		
mm	mm	mm	kPa		
			90	80	70
			Mass flow rate 10^{-5} kg/s		
0.69	24.2	3.2	3.89	5.43	6.44
0.69	24.2	3.4	4.33	5.96	6.95
0.69	24.2	3.6	4.48	6.12	7.08
0.69	32.2	3.2	3.78	5.31	6.33
0.69	32.2	3.4	4.28	5.90	6.91
0.69	32.2	3.6	4.48	6.12	7.07
0.77	16.2	3.2	4.75	6.61	7.85
0.77	16.2	3.4	5.40	7.41	8.70
0.77	16.2	3.6	5.66	7.73	8.96
0.77	24.2	3.2	4.69	6.55	7.78
0.77	24.2	3.4	5.31	7.34	8.59
0.77	24.2	3.6	5.63	7.69	8.92
0.77	32.2	3.2	4.45	6.27	7.45
0.77	32.2	3.4	5.22	7.25	8.55
0.77	32.2	3.6	5.64	7.75	8.97

Table E.2 RANS4 CFD results: Pressure force F_P

d	L	D	p_2		
mm	mm	mm	kPa		
			90	80	70
			Pressure force 10^{-3} N		
0.59	16.2	3.2	4.17	8.00	12.1
0.59	16.2	3.4	2.09	3.96	5.89

Table E.2 RANS4 CFD results: Pressure force F_P

d	L	D	p_2		
mm	mm	mm	kPa		
			90	80	70
			Pressure force 10^{-3} N		
0.59	16.2	3.6	1.10	2.03	3.00
0.59	24.2	3.2	5.03	9.43	14.2
0.59	24.2	3.4	2.55	4.76	7.06
0.59	24.2	3.6	1.38	2.51	3.68
0.59	32.2	3.2	5.87	10.9	16.3
0.59	32.2	3.4	2.97	5.44	8.02
0.59	32.2	3.6	1.55	2.72	3.98
0.69	16.2	3.2	6.42	12.5	19.2
0.69	16.2	3.4	3.55	6.79	10.2
0.69	16.2	3.6	1.99	3.86	5.75
0.69	24.2	3.2	7.57	14.6	22.1
0.69	24.2	3.4	4.12	7.81	11.7
0.69	24.2	3.6	2.28	4.32	6.70
0.69	32.2	3.2	8.54	16.3	25.1
0.69	32.2	3.4	4.66	8.77	13.3
0.69	32.2	3.6	2.62	4.83	7.19
0.77	16.2	3.2	8.41	16.7	26.1
0.77	16.2	3.4	5.02	9.80	15.0
0.77	16.2	3.6	2.98	5.87	8.98
0.77	24.2	3.2	9.85	19.1	29.5
0.77	24.2	3.4	5.61	10.9	16.6
0.77	24.2	3.6	3.47	6.58	9.91

Table E.2 RANS4 CFD results: Pressure force F_P

d	L	D	p_2		
mm	mm	mm	kPa		
			90	80	70
			Pressure force 10^{-3} N		
0.77	32.2	3.2	10.8	21.0	31.9
0.77	32.2	3.4	6.30	12.2	18.6
0.77	32.2	3.6	3.89	7.46	11.1

Table E.3 RANS4 CFD results: Viscous force F_V

d	L	D	p_2		
mm	mm	mm	kPa		
			90	80	70
			Viscous force 10^{-3} N		
0.59	16.2	3.2	0.729	1.31	1.88
0.59	16.2	3.4	0.485	0.868	1.24
0.59	16.2	3.6	0.368	0.671	0.964
0.59	24.2	3.2	0.942	1.67	2.43
0.59	24.2	3.4	0.621	1.10	1.57
0.59	24.2	3.6	0.466	0.829	1.19
0.59	32.2	3.2	1.15	2.02	2.93
0.59	32.2	3.4	0.759	1.33	1.89
0.59	32.2	3.6	0.543	0.951	1.36
0.69	16.2	3.2	1.02	1.83	2.72
0.69	16.2	3.4	0.703	1.21	1.73
0.69	16.2	3.6	0.545	0.991	1.44
0.69	24.2	3.2	1.31	2.36	3.42
0.69	24.2	3.4	0.878	1.56	2.25

Table E.3 RANS4 CFD results: Viscous force F_V

d	L	D	p_2		
mm	mm	mm	kPa		
			90	80	70
			Viscous force 10^{-3} N		
0.69	24.2	3.6	0.685	1.22	1.83
0.69	32.2	3.2	1.56	2.81	4.16
0.69	32.2	3.4	1.08	1.88	2.75
0.69	32.2	3.6	0.80	1.43	2.05
0.77	16.2	3.2	1.25	2.29	3.36
0.77	16.2	3.4	0.88	1.66	2.42
0.77	16.2	3.6	0.73	1.31	1.89
0.77	24.2	3.2	1.64	2.97	4.32
0.77	24.2	3.4	1.14	2.06	3.06
0.77	24.2	3.6	0.90	1.61	2.33
0.77	32.2	3.2	1.91	3.49	5.08
0.77	32.2	3.4	1.33	2.39	3.47
0.77	32.2	3.6	1.08	1.94	2.78